

BOSTON UNIVERSITY
COLLEGE OF ENGINEERING

Thesis

**STUDY OF THE TEMPERATURE DEPENDENT ELECTRON
MOBILITY IN GAN/SCALN HETEROSTRUCTURES**

by

BO-SHIANG YANG

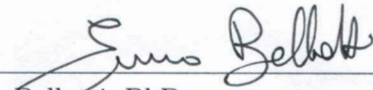
B.S., National Yang Ming Chiao Tung University, 2023

Submitted in partial fulfillment of the
requirements for the degree of
Master of Science

2025

Approved by

First Reader



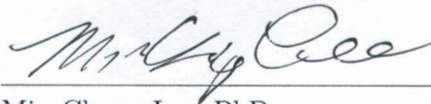
Enrico Bellotti, PhD
Professor of Electrical and Computer Engineering
Professor of Materials Science and Engineering

Second Reader



Sahar Sharifzadeh, PhD
Associate Professor of Electrical and Computer Engineering
Associate Professor of Materials Science and Engineering
Associate Professor of Chemistry

Third Reader



Min-Chang Lee, PhD
Professor of Electrical and Computer Engineering

Acknowledgments

I would like to sincerely thank my thesis advisor, Professor Enrico Bellotti, for his patient guidance, clear explanations, and constant support throughout this research. I've learned so much from him—not just technical knowledge, but also how to approach research with critical thinking and confidence. His help made a big difference in the success of this thesis.

I'm also very grateful to everyone in the Computational Electronics Lab for creating a supportive and friendly environment. I truly appreciated the teamwork, discussions, and encouragement from all of you. Special thanks go to Ze, who gave me valuable guidance on how to design the model; to Luca, who helped me with debugging and coding; and to Catherine, who provided important data for my calculations. Each of you played a key role in helping me complete this work.

To my family, thank you for supporting me from across the world. Your love, encouragement, and belief in me gave me the strength to keep going, even when things were tough. I couldn't have made it through these two years without you.

Finally, I'd like to thank myself—for staying motivated, pushing through challenges, and continuing to learn and grow throughout this journey.

Bo-Shiang Yang

STUDY OF THE TEMPERATURE DEPENDENT ELECTRON MOBILITY IN GAN/SCALN HETEROSTRUCTURES

BO-SHIANG YANG

ABSTRACT

This thesis investigates electron transport in III-nitride heterostructures, comparing AlGaIn/GaN and ScAlN/GaN systems through quantum-mechanical modeling. We examine how polarization effects influence carrier confinement and mobility in these semiconductor interfaces. Our findings reveal that ScAlN/GaN exhibits significantly stronger polarization effects, creating deeper quantum wells and higher sheet carrier densities than AlGaIn/GaN. Despite these enhancements, ScAlN/GaN demonstrates lower electron mobility across all temperatures. Analysis of scattering mechanisms shows that optical phonon scattering dominates at higher temperatures, while interface roughness becomes limiting at lower temperatures, with interface quality critically impacting mobility. These results give an important design trade-off: while ScAlN/GaN offers higher carrier densities for enhanced current capacity, AlGaIn/GaN provides superior carrier mobility for high-frequency applications. This work provides insights for optimizing III-nitride electronic devices for high-power and high-frequency applications.

Contents

1	Introduction	1
2	Methods	4
2.1	Numerical Solution of Poisson and Schrödinger Equation using Finite Difference Method	4
2.1.1	Poisson Equation	5
2.1.2	Schrödinger Equation	6
2.2	Spontaneous and Piezoelectric Polarization Effect	8
2.2.1	Spontaneous Polarization	8
2.2.2	Piezoelectric Polarization	9
2.2.3	Total Polarization and Reduction of Effective Charges	10
2.2.4	Impact on Interface Charge and Device Performance	13
2.3	Self-Consistent Schrödinger-Poisson Solver	13
2.3.1	Initial Conditions and Effective Mass Approximation	13
2.3.2	Self-Consistent Iteration Procedure	14
2.4	Scattering Rate Calculation	17
2.4.1	General Formulation	17
2.4.2	Acoustic Phonon Scattering	19
2.4.3	Interface Roughness Scattering	21
2.4.4	Electron–electron Coulomb Interactions	21
2.4.5	Optical Phonon Scattering	22
2.4.6	Total scattering rate and Mobility	23

3	Results	25
3.1	Results of Self-Consistent Solver for the Heterostructure	25
3.2	Results of Mobility	28
3.2.1	AlGa _N /Ga _N Result	28
3.2.2	ScAl _N /Ga _N Result	34
3.2.3	Comparison between AlGa _N /Ga _N and ScAl _N /Ga _N	37
3.2.4	Interface Roughness Effects on 2DEG Transport	38
4	Conclusions	43
	References	46
	Curriculum Vitae	48

List of Tables

2.1	Parameters of spontaneous polarizaton, piezoelectric, elastic , dielectric constant, effective mass of electron and bandgap (H-Hexagonal, ZB- Zincblende)	15
2.2	Parameters used in the mobility calculation(Yu and Brennan, 2001; Hsu and Walukiewicz, 1997)	24

List of Figures

2.1	Numerically Solution of Poisson Equation of Heterostructure ScAlN/GaN .	6
2.2	Numerical Solution of Schrödinger Equation of Heterostructure ScAlN/GaN	8
2.3	Spontaneous Polarization of $Sc_xAl_{1-x}N$ and GaN (lh: layered-hexagonal, zb: Zinc-Blende structure)	9
2.4	Piezoelectric Polarization of $Sc_xAl_{1-x}N/GaN$, using layered-hexagonal as the reference structure.	11
2.5	Polarization-induced Sheet Charges of $Al_xGa_{1-x}N/GaN$	11
3.1	Conduction Band Energy of $Al_{0.15}Ga_{0.85}N/GaN$ at 300K	26
3.2	The Lowest Point of Conduction Band in $Al_{0.15}Ga_{0.85}N/GaN$	26
3.3	Conduction Band Energy of $Sc_{0.18}Al_{0.82}N/GaN$ at 300K	26
3.4	The Lowest Point of Conduction Band in $Sc_{0.18}Al_{0.82}N/GaN$	26
3.5	Ground State Wave Function of AlGaN/GaN at 300K	27
3.6	Ground State Wave Function of ScAlN/GaN at 300K	27
3.7	Conduction Band Energy with First Five Subband Energy of AlGaN/GaN at 50K	27
3.8	Conduction Band Energy with First Five Subband Energy of ScAlN/GaN at 150K	27
3.9	Mobility of $AlGaN/GaN$ under different temperature, where "." is the experimental data.	29

3·10	Scattering Rate of AlGa _N /Ga _N at 300K: (a)Deformation Potential (b)Piezoelectric Phonon (c)Emission of LO phonon (d)Absorption of LO phonon (e)Interface Roughness, the Electron Energy is measured from the bottom of the first subband to second subband	31
3·11	Mobility of ScAl _N /Ga _N under different temperature, where "." is the experimental data	33
3·12	Scattering Rate of ScAl _N /Ga _N at 300K: (a)Deformation Potential (b)Piezoelectric Phonon (c)Emission of LO phonon (d)Absorption of LO phonon (e)Interface Roughness, the Electron Energy is measured from the bottom of the first subband to second subband	36
3·13	Interface Roughness mobility with different parameter Δ and \wedge in AlGa _N /Ga _N	38
3·14	Effect of Roughness Height on Mobility (300K) of AlGa _N /Ga _N Interface .	40
3·15	Effect of Correlation Length on Mobility (300K) of AlGa _N /Ga _N Interface .	40
3·16	Effect of Roughness Height on Mobility (300K) of ScAl _N /Ga _N Interface .	41
3·17	Effect of Correlation Length on Mobility (300K) of ScAl _N /Ga _N Interface .	41

List of Abbreviations

DP	Deformation Potential
e	elementary charge ($1.6 * 10^{-19} C$)
LO	Longitudinal Optical
PZ	Piezoelectric

Chapter 1

Introduction

Wide-bandgap III-nitride compounds within semiconductor heterostructures play a crucial role in modern advanced electronic devices. AlGaN/GaN and ScAlN/GaN materials demonstrate significant potential for electronic systems requiring high power output along with high frequency and temperature tolerance. The special properties of these materials fulfill the rising demand for electronic components with both improved efficiency and extended durability. The natural polarization effects in III-nitride heterostructures generate electric fields which have a significant impact on electron behavior inside the device. Lattice constant variations among these heterostructure compounds generate spontaneous and piezoelectric polarization which significantly impacts the electron dynamics at semiconductor interfaces. The formation of a two-dimensional electron gas (2DEG) confined to the quantum well at the interface arises from polarization effects together with band gap differences that lead to discontinuities in the conduction band. Within this quantum well electrons are restricted to one dimension but maintain freedom to move in the remaining two dimensions thus forming a high-mobility channel. Electrons accumulate in the quantum well through polarization-induced sheet charges at the interface which serves as a key factor for efficient electronic device operation.

For high-electron-mobility transistors (HEMTs), AlGaN/GaN has served as the traditional standard among III-nitride materials. Introducing scandium to aluminum nitride for the formation of ScAlN/GaN structures demonstrates potential for enhanced device performance. The mismatch in lattice dimensions between GaN and compounds such as AlGaN

or ScAlN generates strain-induced polarization fields which alter energy band bending and modify carrier concentration. The interface between ScAlN and GaN generates a high-density two-dimensional electron gas (2DEG) due to the difference in polarization. Despite these benefits, several factors limit how well electrons can move in these systems: Three main factors limit electron mobility in these systems through roughness at material interfaces and acoustic phonon scattering which includes impurity effects, deformation potential and piezoelectric mechanisms along with polar optical phonon scattering.

The different scattering mechanisms determine the effects on mobility and the total scattering rate is a sum from all mechanisms. The rate of total scattering limits the performance of devices. In 2DEG systems, deformation potential scattering takes place when electrons are actively moving on top of an acoustic phonon lattice through strain fields. The piezoelectric scattering is due to the electric fields produced in polar materials from lattice vibrations—phonon coupling called piezoelectric effect. The interface roughness scattering is significant when electrons are colliding on the boundary between two materials. Optical phonon scattering is strong in room temperature where electrons emit or absorb energy from or to high frequency of vibration of the lattice.

Understanding these transport phenomena involves an approach to quantum mechanics. This computation requires the self-consistent framework of the Poisson and Schrödinger equations to properly model the 2DEG formation and its characteristics. The Poisson equation calculates the electrostatic potential due to a charge distribution which also accounts for polarization charges while the Schrödinger equation determines the distribution of the conduction band electrons. These equations yield important information on the occupation of the electronic levels, the charge density, and the degree of band bending at the interface. Regarding the ScAlN/GaN heterostructures, enhanced polarization effects give rise to stronger band bending and, hence, higher 2DEG densities, which improves device performance parameters.

In order to determine the transport properties, we first obtain the relaxation time from the various scattering mechanisms to compute electron mobility. Each mechanism—polar optical phonon scattering, deformation potential, piezoelectric acoustic phonons, and interface roughness—has associated with it the different energy-dependent scattering rates which are obtained by solving the appropriate matrix elements with the wavefunctions using the Schrödinger equation. The mobility is calculated using the relaxation time approximation. We are able to model carrier transport phenomena under a wide range of temperatures and structural parameters, which provides important information for improving device performance, by employing this approach through numerical integration of energy-dependent scattering rates and the Fermi-Dirac distribution's derivative.

This thesis analyzes, using a broad numerical approach, the electron transport features of 2DEGs at the III-nitride heterointerfaces focusing on ScAlN/GaN systems. The goal of this work is to compute the electron mobility as a function of temperature and to explain the fundamental physics of carrier transport in these complex semiconductor structures by developing appropriate scattering mechanisms and solving the coupled Poisson-Schrödinger equations using finite difference methods. This research aims at the development of high performance electronic devices incorporating power electronics and RF communications by understanding the enhancement and factors of electron mobility within ScAlN/GaN heterostructures.

Chapter 2

Methods

In our study of electron transport in semiconductor heterostructures, we chose the effective mass approximation (EMA) as our main modeling approach. While other methods like density functional theory could provide more detail at the atomic level, they would require too much computational power when modeling entire device structures. The effective mass approximation gives us a good balance between accuracy and computational efficiency. It properly captures the key physics we need to understand—how energy bands bend, how quantum wells form, and how electrons distribute at interfaces between materials. These factors directly affect electron scattering and mobility, which are important to our research comparing AlGaIn/GaN and ScAlIn/GaN systems. We'll explain the details of how we implemented this approach in later sections.

2.1 Numerical Solution of Poisson and Schrödinger Equation using Finite Difference Method

The accurate modeling of quantum confinement and carrier distribution in semiconductor heterostructures requires a self-consistent solution of the Poisson and Schrödinger equations. In this work, both equations are discretized using the finite difference method (FDM), thereby converting the continuous differential equations into a set of algebraic equations that can be solved numerically.

2.1.1 Poisson Equation

The Poisson equation describes the electrostatic potential, $\phi(z)$, which arises from the distribution of charges within the heterostructure. In its general form, the Poisson equation is expressed as

$$\nabla^2 \phi(z) = -\frac{q\rho(z)}{\epsilon_0 \epsilon_r(z)} \quad (2.1)$$

where q is the elementary charge, ϵ_0 is the vacuum permittivity, and $\epsilon_r(z)$ is the position-dependent relative permittivity. The charge density, $\rho(z)$, includes contributions from ionized donors (N_d^+), ionized acceptors (N_a^-), free carriers (electrons, n , and holes, p), as well as polarization-induced charges (ρ_{pol}). In expanded form, the equation becomes

$$\nabla^2 \phi(z) = -\frac{q}{\epsilon_0 \epsilon_r(z)} (N_d^+ - N_a^- + p - n + \rho_{pol}). \quad (2.2)$$

To solve this equation numerically, the second derivative (the Laplacian operator) is approximated using a second-order central difference scheme.[\(Zaman, 2022\)](#) For a uniform grid with spacing Δz , the second derivative at node i is approximated by

$$\frac{\partial^2 \phi_i}{\partial z^2} \approx \frac{\phi_{i-1} - 2\phi_i + \phi_{i+1}}{(\Delta z)^2}. \quad (2.3)$$

This discretization transforms the Poisson equation into a linear system of equations that can be represented in matrix form:

$$\frac{1}{(\Delta z)^2} \begin{bmatrix} -2 & 1 & 0 & \cdots & 0 \\ 1 & -2 & 1 & \cdots & 0 \\ 0 & 1 & -2 & \cdots & 0 \\ \vdots & \vdots & \vdots & \ddots & \vdots \\ 0 & 0 & 0 & \cdots & -2 \end{bmatrix} \begin{bmatrix} \phi_1 \\ \phi_2 \\ \vdots \\ \phi_{N-1} \\ \phi_N \end{bmatrix} = \begin{bmatrix} b_1 \\ b_2 \\ \vdots \\ b_{N-1} \\ b_N \end{bmatrix}, \quad (2.4)$$

where the right-hand side vector b contains the discretized charge density term:

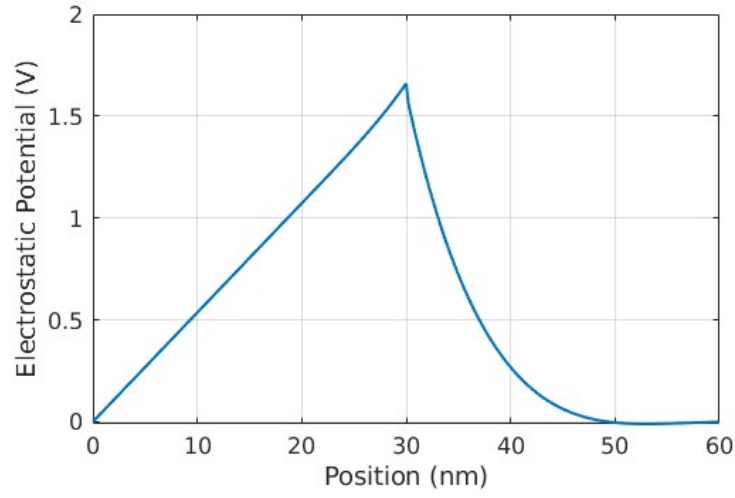


Figure 2.1: Numerically Solution of Poisson Equation of Heterostructure ScAlN/GaN

$$b_i = -\frac{q}{\epsilon_0 \epsilon_r(z_i)} (N_d^+ - N_a^- + p - n + \rho_{pol}). \quad (2.5)$$

Thus, the Poisson equation is transformed into a linear system of the form:

$$A\phi = b, \quad (2.6)$$

where A is the tridiagonal matrix representing the finite difference discretization. This system can be efficiently solved using numerical linear algebra techniques. The solution is shown in Figure 2.1. The Figure shows significant band bending near the interface, where the polarization charges creates a potential well. This well confines the two-dimensional electron gas (2DEG), with the potential gradient driving carrier accumulation at the interface.

2.1.2 Schrödinger Equation

The Schrödinger equation, which represents the quantum behavior of electrons in the conduction band, is similarly discretized. In one dimension, the Schrödinger equation for

an electron with position-dependent effective mass, $m^*(z)$, and potential energy, $V(z)$, is written as

$$\left[-\frac{\hbar^2}{2m^*(z)} \nabla^2 + V(z) \right] \psi_n(z) = E_n \psi_n(z), \quad (2.7)$$

where \hbar is the reduced Planck constant, $\psi_n(z)$ is the wave function corresponding to the n -th energy eigenstate, and E_n is the associated eigenenergy. The second derivative in this equation is approximated using the same finite difference approach as for the Poisson equation, yielding a discrete eigenvalue problem. (Halpern et al., 2022) In matrix form, the Hamiltonian operator becomes

$$\left\{ -\frac{\hbar^2}{2m^*(z)} \frac{1}{(\Delta z)^2} \begin{bmatrix} -2 & 1 & 0 & \cdots & 0 \\ 1 & -2 & 1 & \cdots & 0 \\ 0 & 1 & -2 & \cdots & 0 \\ \vdots & \vdots & \vdots & \ddots & \vdots \\ 0 & 0 & 0 & \cdots & -2 \end{bmatrix} + I_n V(z) \right\} [\psi_n(z)] = E_n [\psi_n(z)], \quad (2.8)$$

where I_n is the identity matrix, and $V(z)$ is the potential energy matrix. This formulation transforms the Schrödinger equation into an eigenvalue problem, which can be solved numerically using matrix diagonalization methods. The solution of eigenfunction is shown in Figure 2.2. The solutions to the Schrödinger equation in heterostructure quantum wells look a lot like Airy functions, especially near the interface. This happens because polarization effects in materials like ScAlN/GaN create band bending that forms something very close to a triangular potential well. The resemblance is strongest for the ground state and first few excited states, which are mostly confined close to the interface where the potential is most triangular-shaped. For a perfect triangular well, Airy functions are the exact analytical solution. This is why many analytical models of 2DEG often use Airy function as approximation.

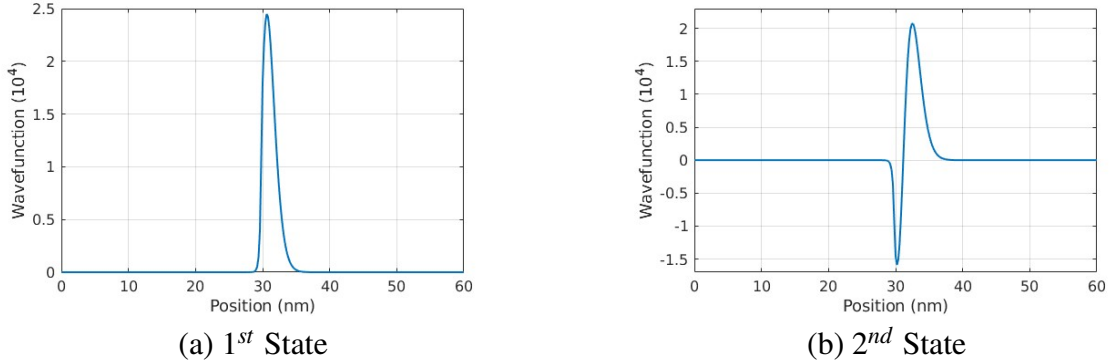


Figure 2-2: Numerical Solution of Schrödinger Equation of Heterostructure ScAlN/GaN

2.2 Spontaneous and Piezoelectric Polarization Effect

Polarization play a critical role in determining the electrical and piezoelectric properties of III-nitride heterostructures. In wurtzite-structured materials such as AlN and GaN, the total polarization is composed of two primary components: spontaneous polarization, P_{sp} , which arises intrinsically from the lack of inversion symmetry in the crystal lattice, and piezoelectric polarization, P_{pe} , which is induced by strain resulting from lattice mismatches. The incorporation of scandium (Sc) into AlN to form ScAlN dramatically enhances both components, leading to significant interface effects when ScAlN is paired with GaN in heterostructures.

2.2.1 Spontaneous Polarization

Spontaneous polarization is an inherent property of the wurtzite crystal structure and increases with the degree of lattice distortion and ionic character. In ScAlN, the introduction of Sc atoms generates additional strain within the lattice, resulting in a substantial enhancement of P_{sp} . When the layered-hexagonal lattice is used as the reference structure—shown to yield better agreement with experimental data compared to the zinc-blende reference—the spontaneous polarization of $Sc_{0.15}Al_{0.85}N$ is estimated to be approximately

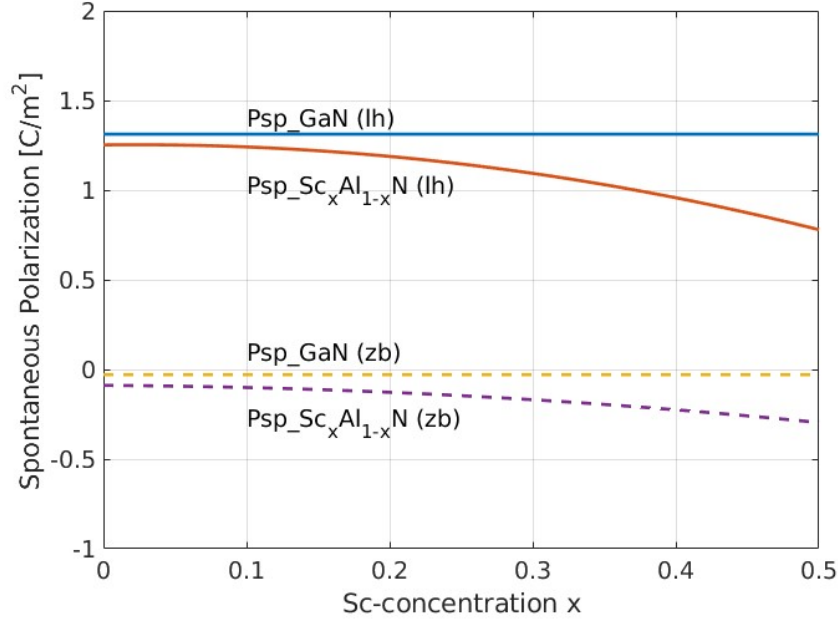


Figure 2-3: Spontaneous Polarization of $Sc_xAl_{1-x}N$ and GaN (lh: layered-hexagonal, zb: Zinc-Blende structure)

1.248 C/m², as shown in Figure 2-3.(Yassine et al., 2024) This value is significantly larger than the spontaneous polarization observed in GaN, which is around 0.028 C/m².

2.2.2 Piezoelectric Polarization

In hexagonal ScAlN/GaN heterostructures, the crystal structure lacks inversion symmetry along the c -axis. As a result, any distortion in the crystal lattice can induce or modify an electric dipole, giving rise to piezoelectric polarization in addition to the spontaneous polarization P_{sp} . Specifically, when a ScAlN barrier is grown epitaxially on GaN in the c -plane (i.e., along [0001]), the lattice mismatch imposes biaxial in-plane stress ($\sigma_1 = \sigma_2, \sigma_3 = 0$, where σ means stress), since the film is free to relax in the out-of-plane direction([0001]) but is forced to match GaN in-plane(x - y plane). Hooke's law and the 6×6 stiffness matrix $\{C_{ij}\}$ yield (Ambacher et al., 1999)

$$\sigma_3 = C_{13}\epsilon_1 + C_{23}\epsilon_2 + C_{33}\epsilon_3 = 2C_{13}\epsilon_1 + C_{33}\epsilon_3 = 0, \quad (2.9)$$

which implies

$$\epsilon_3 = -\frac{2C_{13}}{C_{33}}\epsilon_1. \quad (2.10)$$

Because of the hexagonal symmetry and lack of inversion center, this in-plane strain ϵ_1 ($=\epsilon_2$) couples to an out-of-plane polarization:

$$P_{pe} = e_{31}\epsilon_1 + e_{32}\epsilon_2 + e_{33}\epsilon_3 = 2e_{31}\epsilon_1 + e_{33}\epsilon_3 = 2\epsilon_1 \left(e_{31} - e_{33} \frac{C_{13}}{C_{33}} \right), \quad (2.11)$$

where e_{31}, e_{32}, e_{33} are the piezoelectric constants, and C_{13}, C_{33} are corresponding elastic stiffness coefficients. Here, the in-plane strain ϵ_1 is determined by the lattice mismatch,

$$\epsilon_1 = \frac{a_{\text{buffer}} - a_{\text{barrier}}}{a_{\text{barrier}}}, \quad (2.12)$$

with a_{buffer} and a_{barrier} being the in-plane lattice constants of GaN and ScAlN, respectively. Hence, the combination of no inversion symmetry and biaxial in-plane stress in hexagonal ScAlN/GaN results in a net piezoelectric polarization P_{pe} along the $[0001]$ axis, which adds to the spontaneous polarization P_{sp} , thus forming the total out-of-plane polarization:

$$P_t = P_{sp} + P_{pe}.$$

This polarization directly governs charge distributions, carrier confinement, and electrical behavior in ScAlN/GaN devices.

2.2.3 Total Polarization and Reduction of Effective Charges

The total macroscopic polarization in a heterostructure, defined as

$$P_t = P_{sp} + P_{pe}, \quad (2.13)$$

represents the sum of the spontaneous polarization, P_{sp} , and the piezoelectric polarization, P_{pe} , induced by lattice strain. In ScAlN/GaN heterostructures, the incorporation of scan-

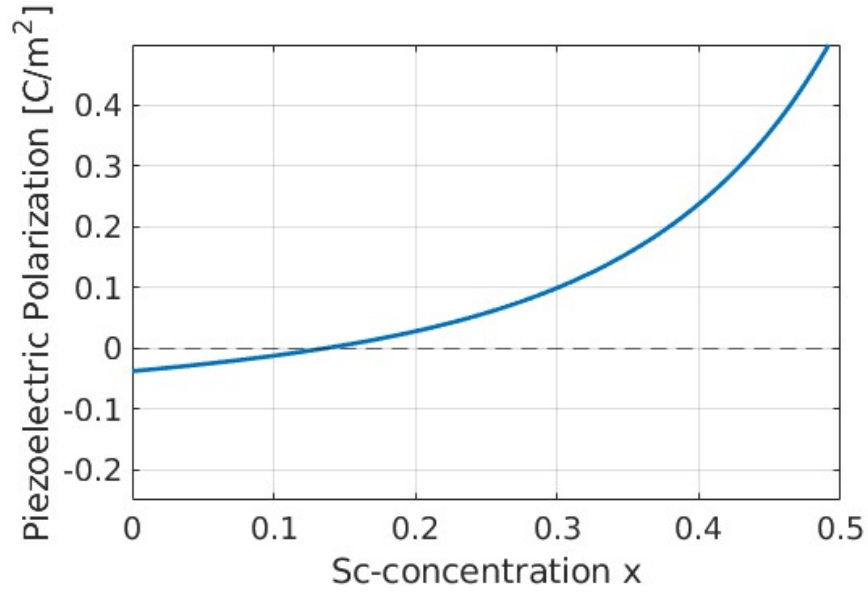


Figure 2.4: Piezoelectric Polarization of $Sc_xAl_{1-x}N/GaN$, using layered-hexagonal as the reference structure.

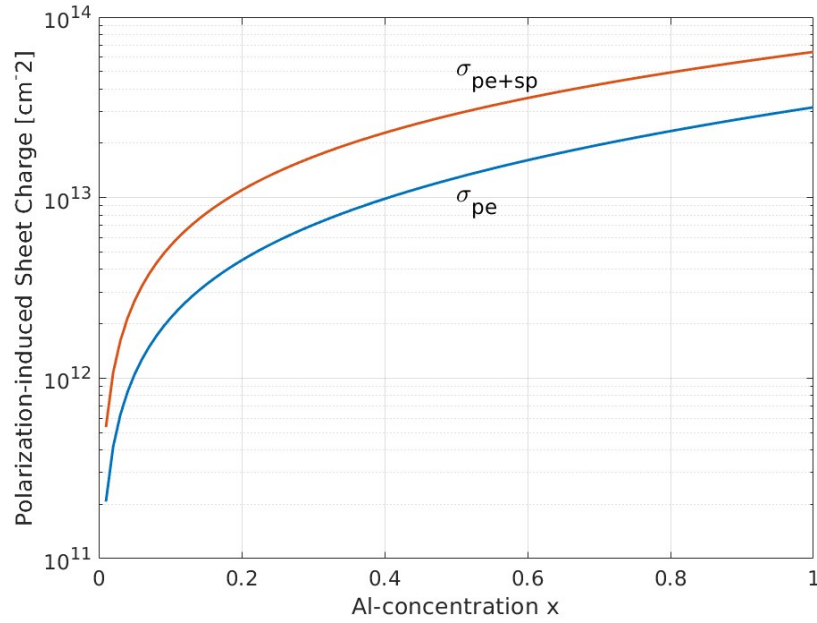


Figure 2.5: Polarization-induced Sheet Charges of $Al_xGa_{1-x}N/GaN$

dium (Sc) in AlN substantially enhances P_{sp} (e.g., up to 1.248 C/m² for $Sc_{0.15}Al_{0.85}N$) compared to GaN (approximately 0.028 C/m²). Additionally, the lattice mismatch between ScAlN and GaN gives rise to a significant P_{pe} , calculated via

$$P_{pe} = 2\varepsilon_1 \left(e_{31} - e_{33} \frac{C_{13}}{C_{33}} \right), \quad (2.14)$$

where ε_1 is the in-plane strain, and e_{31} , e_{33} , C_{13} , and C_{33} are the piezoelectric and elastic constants, respectively. The polarization-induced sheet charges of AlGaIn/GaN are shown in Figure 2.5 (Ambacher et al., 2000)

However, the macroscopic polarization difference between the layers, when calculated without further refinement, tends to overestimate the interface sheet charge. This discrepancy arises because the absolute polarization of a crystal is only defined modulo a quantum, a concept central to the modern theory of polarization (MTP). In the microscopic approach, the formal polarization P_f is multivalued, and only the difference between two formal polarizations is physically meaningful. As a result, cancellations occur due to the periodicity of the polarization lattice, and the effective (or microscopic) polarization charge, σ_{micro} , is given by

$$\sigma_{micro} = \sigma_{macro} + 2\varepsilon_1 P_f^{w,top} \quad (2.15)$$

Thus, even though the total polarization P_t from Eq. (2.13) may be very high, the effective polarization-induced sheet charge at the heterointerface is reduced by these microscopic cancellation effects. In practice, this means that the net polarization charge, which governs the band bending and the formation of a two-dimensional electron gas (2DEG) in devices such as high-electron-mobility transistors (HEMTs), is lower than what would be predicted by a simple macroscopic difference. (Yassine et al., 2024)

2.2.4 Impact on Interface Charge and Device Performance

The large difference in polarization between ScAlN and GaN, driven by the enhanced P_{sp} in ScAlN and further modified by P_{pe} due to biaxial strain, leads to a significant polarization discontinuity at the heterointerface. This discontinuity manifests as a bound sheet charge that greatly influences the band bending and carrier confinement in the structure. Enhanced polarization fields result in a narrower two-dimensional electron gas (2DEG) channel and increase the sensitivity of the channel electrons to interface roughness scattering, thereby affecting the overall electron mobility. Such effects are critical in the design of high-electron-mobility transistors (HEMTs) and other III-nitride-based devices, where precise control over polarization-induced charge is essential for optimizing performance.

2.3 Self-Consistent Schrödinger-Poisson Solver

The electronic properties of semiconductor heterostructures, such as the band structure and carrier distribution, can be accurately described through a self-consistent Schrödinger-Poisson solver. This computational framework is essential for modeling quantum confinement effects in low-dimensional systems, particularly for the formation of two-dimensional electron gases (2DEG) in heterostructures such as AlGaIn/GaN and ScAlN/GaN. The solution to this problem requires a self-consistent approach, where the Schrödinger equation determines the wave functions and energy states of confined electrons, while the Poisson equation accounts for the electrostatic potential due to charge redistribution. (Gunna et al., 2007)

2.3.1 Initial Conditions and Effective Mass Approximation

To initiate the self-consistent cycle, an initial guess for the conduction band is required. The reference Fermi level is chosen to be zero throughout the entire structure, establishing a common energy reference for subsequent calculations. Given the complexity of directly

solving the Schrödinger equation in a crystal lattice with a periodic potential, the effective mass approximation (EMA) is employed to simplify the Hamiltonian.

The potential energy of an electron within a periodic crystal structure consists of contributions from the atomic cores and the surrounding electronic cloud. However, explicitly incorporating this periodic potential into the Schrödinger equation would necessitate a computational grid smaller than the lattice constant, making the numerical solution intractable. To circumvent this issue, the effective mass approximation replaces the periodic potential with a modified kinetic term that accounts for band structure effects (Chuang, 2009). Under this approximation, the Hamiltonian for a quantum well system, such as AlGaIn/GaN, is expressed as:

$$H = -\frac{\hbar^2}{2m_c^*}\nabla^2 + E_c(k=0), \quad (2.16)$$

where m_c^* is the effective conduction band mass, and $E_c(k=0)$ represents the conduction band minimum. By adopting this formulation, the periodic potential is effectively absorbed into the band parameters, allowing for larger grid spacing in numerical calculations without sacrificing accuracy. This significantly improves computational efficiency while maintaining physical accuracy.

2.3.2 Self-Consistent Iteration Procedure

The solution process begins with an initial conduction band profile, which serves as the starting point for solving the Schrödinger equation. Since the Fermi level is assumed to be uniform throughout the structure ($E_f = 0$), discontinuities may arise at material interfaces due to differences in conduction band alignment. To accurately model these discontinuities, double-node representation is employed at the heterointerface, ensuring continuity in both the wave function and its derivative while preserving the material-specific band offsets.

Once the eigenstates and corresponding wave functions are determined, the electron

Parameter	$Al_xGa_{1-x}N$	$Sc_xAl_{1-x}N$	GaN
$P_{sp} (C/m^2)$	$-0.052x - 0.029$	$-0.646x^2 - 0.315x + 1.315$	1.312 (H Ref) -0.029 (ZB Ref)
$e_{33} (C/m^2)$	$(1.46 - 0.73)x + 0.73$	$1.47(1 + 0.7x + 4.5x^2)$	0.73
$e_{31} (C/m^2)$	$(-0.6 + 0.49)x - 0.49$	$-0.6(1 + 0.3x + 0.97x^2)$	-0.49
$C_{31} (GPa)$	$5x + 103$	$100(1 + 0.8x - 0.48x^2)$	103
$C_{33} (GPa)$	$-32x + 405$	$352(1 - 1.16x - 0.256x^2)$	405
$\epsilon (\epsilon_0)$	10.355	11.271	9.7
$m_n (m_0)$	0.22	0.27	0.19
$E_g (eV)$	3.82	4.05	3.4

Table 2.1: Parameters of spontaneous polarizaton, piezoelectric, elastic , dielectric constant, effective mass of electron and bandgap (H-Hexagonal, ZB- Zincblende)

density is computed using the Fermi-Dirac distribution:

$$n^k = DOS_{2D} * \sum_j |\psi_j|^2 \mathcal{F}_0\left(\frac{Ec - Ef}{k_B T}\right), \quad (2.17)$$

where $\psi_i(z)$ represents the wave function of the i -th subband, $\mathcal{F}_0(x)$ is the Fermi-Dirac integral of order 0, which is equal to $\ln(1 + \exp(x))$, and $DOS_{2D} = (m^* k_B T) / (\pi \hbar)$. The obtained electron density is then used as input for the Poisson equation, which governs the electrostatic potential distribution:

$$\nabla^2 V = -\frac{q\rho}{\epsilon} \quad (2.18)$$

where ϵ is the permittivity, V is the electrostatic potential, and ρ represents the charge density, including both free carriers and ionized dopants. The newly computed potential modifies the conduction band profile, which is subsequently used to update the Schrödinger equation. This iterative process continues until self-consistency is achieved, meaning that successive iterations result in negligible changes to the electron density and potential.

([Gunna et al., 2007](#))

The self-consistent loop is solved in this order: (**i** stands for nodes; **k** stands for iteration)

1. Solve Poisson Equation to obtain the electrostatic potential ϕ_i^k

$$\nabla^2 \phi_i^k(z) = \frac{-q}{\epsilon_0 \epsilon_r(z)} (Nd^+ - Na^- + p - n^{(k)} + \rho_{pol}) \quad (2.19)$$

2. Add the electrostatic potential to the conduction band E_c

$$E_c = -q\phi_i^k + \Delta E_c \quad (2.20)$$

3. Solve Schrödinger equation to determine the wavefunction ψ_i^k

$$\left[-\frac{\hbar^2}{2m_c^*(z)} \nabla^2 + E_c(z) \right] \psi_i^k(z) = E_i^k \psi_i^k(z) \quad (2.21)$$

4. Use the Fermi-Direc distribution to calculate the electron concentration n^k

$$n_i^k = DOS_{2D} * \sum_j |\psi_j|^2 \mathcal{F}_0\left(\frac{E_{ci} - E_f}{k_B T}\right) \quad (2.22)$$

5. Under-Relaxation Approximation for the electron concentration n^k

$$n_i^k = \omega n_i^k + (1 - \omega) n_i^{k-1} \quad (2.23)$$

6. Check if the electron concentration converges

$$\frac{n_i^k - n_i^{k-1}}{n_i^{k-1}} < \epsilon \quad (2.24)$$

The loop ends when the electron concentration at all nodes reaches convergence. The parameters needed for the self-consistent solver is listed in [Table 2.1](#).

2.4 Scattering Rate Calculation

In our methods, we consider the scattering events due to (1) the acoustic phonon, which includes the deformation potential, longitudinal piezoelectric and transverse piezoelectric phonon, (2) polar optical phonon and (3) interface roughness.

2.4.1 General Formulation

The scattering rate can be determined by the Boltzmann equation:

(Kawamura and Das Sarma, 1992)

$$\frac{\partial f}{\partial t} = -\frac{1}{\hbar} \frac{\partial E}{\partial \mathbf{k}} \cdot \frac{\partial f}{\partial \mathbf{r}} - \frac{1}{\hbar} \mathbf{F} \cdot \frac{\partial f}{\partial \mathbf{k}} + I(f) \Big|_{\text{collision}}, \quad (2.25)$$

where f is the distribution function, E is the electron energy, and \mathbf{F} is the external electric field. $I(f)$ is the collision integral, which arises from electron scattering and can be written as:

$$I(f) = \int [f_{k'}(1 - f_k)W(k', k) - f_k(1 - f_{k'})W(k, k')] \frac{d^3 k'}{(2\pi)^3}, \quad (2.26)$$

where $W(k', k)$ is the transition rate from state $|k'\rangle$ to state $|k\rangle$, which can be obtained using the "Fermi Golden Rule": (Bransden et al., 2000)

$$W(k', k) = \frac{2\pi}{\hbar} |C_{k'k}|^2 \delta(E(k) - E(k') - \hbar\omega). \quad (2.27)$$

The matrix element $C_{k'k}$ for the transition from $|k'\rangle$ to $|k\rangle$ is given by:

$$C_{k'k} = \int_V \Psi_{k'}^* C \Psi_k d^3 r, \quad (2.28)$$

where the scattering potential C is determined by the specific scattering mechanism.

Under the assumption of a uniform electric field in a homogeneous system, the Boltzmann equation simplifies to:

$$\frac{1}{\hbar} \mathbf{F} \cdot \frac{\partial f}{\partial \mathbf{k}} = I(f) \Big|_{\text{collision}}. \quad (2.29)$$

In equilibrium, the carrier distribution is given by the Fermi-Dirac distribution f_0 . In the presence of an external electric field, the carrier distribution f can be expanded using Legendre polynomials. For low electric fields, we can approximate f as:

$$f(\mathbf{k}) \simeq f_0 - \frac{e\hbar}{m^*} F k \cos \Phi \frac{\partial f_0}{\partial E} \phi(E), \quad (2.30)$$

where f_0 is the equilibrium Fermi-Dirac distribution, Φ is the angle between \mathbf{k} and \mathbf{F} , m^* is the isotropic effective mass of the carriers, and $\phi(E)$ (with units of s^{-1}) is the small-perturbation distribution due to the external electric field, in order to describe the non-equilibrium deviation of the electron distribution.

Using the principle of detailed balance, where the rate of the forward process is exactly equal to the rate of the reverse process, i.e. the scattering rate from $|k'\rangle$ to $|k\rangle$ is same as from $|k\rangle$ to $|k'\rangle$, the transition rates satisfy:

$$W(k', k) f_0(E') [1 - f_0(E)] = W(k, k') f_0(E) [1 - f_0(E')] \quad (2.31)$$

Therefore, we can rewrite equation 2.26, using equation 2.31, 2.30 and the expression of equilibrium Fermi-Direc distribution f_0 , as

$$\begin{aligned} I(f) = & -\frac{e\hbar}{m^* k_B T} F k \cos \Phi \\ & * \int \frac{d^3 k'}{(2\pi)^3} f_0(E) [1 - f_0(E')] \\ & * [\phi(E) - \frac{k' \cos \theta}{k} \phi(E')] W(k, k'), \end{aligned} \quad (2.32)$$

where θ is the angle between \mathbf{k} and \mathbf{k}' . Finally, using equation 2.32 and 2.30 into 2.29, we can get the linearized Boltzmann equation:

$$\begin{aligned} 1 = & \int \frac{d^3 k'}{(2\pi)^3} \frac{1 - f_0(E')}{1 - f_0(E)} \\ & * [\phi(E) - \frac{k' \cos \theta}{k} \phi(E')] W(k, k'), \end{aligned} \quad (2.33)$$

where the the perturbation distribution $\phi(E)$ can be calculated in the following section to obtain the relaxation time $\tau(E)$.

2.4.2 Acoustic Phonon Scattering

In acoustic phonon scattering rate, we consider two major mechanism: Deformation Potential (DP) and Piezoelectric (PZ) Scattering. Deformation potential (DP) scattering occurs when electrons interact with the strain field caused by acoustic phonons. The strain modifies the band structure locally, creating a potential that scatters electrons, while Piezoelectric (PE) scattering arises in materials with no inversion symmetry (e.g., ScAlN) due to the electric fields generated by lattice vibrations. These fields interact with electrons, causing scattering.

To account for the screening effect by the 2D electron gas, the electron–phonon interaction potential is modified by a static screening function, (Hsu and Walukiewicz, 1997)

$$S(q) = \frac{q}{q + q_s H_{ij}(q)}, \quad (2.34)$$

where $q = |\mathbf{k} - \mathbf{k}'|$ is the in-plane wavevector transfer between initial and final electron states \mathbf{k} and \mathbf{k}' , $q_s = 2m^*e^2/(\epsilon_s\hbar^2)$ is the screening wavevector, and $H_{ij}(q)$ is the subband coupling coefficient, which is defined as

$$H_{ij}(q) = \iint \psi_i(z_1)\psi_j(z_2)e^{-q|z_1-z_2|}dz_1dz_2 \quad (2.35)$$

Starting from the linearized Boltzmann transport equation (equation 2.33) for the 2D electron gas under acoustic phonon scattering, we can rewrite it as: (Kawamura and

Das Sarma, 1992)

$$\begin{aligned}
 1 = & \frac{1}{(2\pi)^3} \frac{2\pi}{\hbar} \int d^2k' \int dq_z \frac{1 - f_0(E')}{1 - f_0(E)} \\
 & * \left[\phi(E) - \frac{k' \cos \theta}{k} \phi(E') \right] \\
 & * |I(q_z)|^2 |C_j(q, q_z)|^2 S^2(q) \Delta(E, E'),
 \end{aligned} \tag{2.36}$$

where q_z is the phonon wave vector, $I(q_z) = \int \Psi^2(z) e^{iq_z z} dz$ describes the overlap integral for the electron subband wavefunction in the z -direction, $C_j(q, q_z)$ is the matrix elements for deformation potential and piezoelectric scattering, which is defined in (Kawamura and Das Sarma, 1992), and $\Delta(E, E')$ represents energy conservation.

For acoustic phonon scattering at typical experimental conditions ($\hbar\omega_q \ll E_F$, where E_F is the Fermi energy), the scattering processes are effectively quasi-elastic, simplifying the integral. Under this approximation, the equation 2.36 reduces to a simpler integral form for $\tau(E) = \phi(E)$:

$$\begin{aligned}
 \phi^{-1}(E) = & \frac{1}{(2\pi)^3} \frac{2\pi}{\hbar} \int d^2k' \int dq_z (1 - \cos \theta) \\
 & * |I(q_z)|^2 |H_{ij}(q, q_z)|^2 S^2(q) \Delta(E, E'),
 \end{aligned} \tag{2.37}$$

Finally, solving equation 2.37, the scattering rate of deformation potential and piezoelectric scattering can be written as (Kawamura and Das Sarma, 1992; Yoon et al., 1987)

$$\tau_{\text{DP}}^{-1}(E) = \frac{3D^2 m^* k_B T}{16\pi \hbar^3 \rho v_l^2} \int_0^\pi S^2(q) (1 - \cos \theta) d\theta \tag{2.38}$$

$$\tau_{\text{PZ},l}^{-1}(E) = \frac{9}{32} \frac{(e h_{14})^2 m^* k_B T}{2\pi \hbar^3 c_l} \int_0^\pi \frac{S^2(q)}{q} (1 - \cos \theta) f_l(\omega) d\theta \tag{2.39}$$

$$\tau_{\text{PZ},t}^{-1}(E) = \frac{13}{32} \frac{(e h_{14})^2 m^* k_B T}{2\pi \hbar^3 c_t} \int_0^\pi \frac{S^2(q)}{q} (1 - \cos \theta) f_t(\omega) d\theta \tag{2.40}$$

where m^* is the effective electron mass, D is the deformation potential constant, ρ is the

mass density of the crystal, v_l is the longitudinal acoustic phonon velocity, h_{14} is the piezoelectric tensor constant, c_l (c_t) is the longitudinal (transverse) elastic constant in GaN (where $c_{l,t} = \rho v_{l,t}^2$), and dimensionless function $f_l(\omega)$ and $f_t(\omega)$ is the form factors for the acoustic phonon modes, which is defined as:

$$f_l(\omega) = \frac{1}{3} \int dz \int dz' \psi^2(z) \psi^2(z') * (3 + 3u - u^3) e^{-u} \quad (2.41)$$

$$f_t(\omega) = \frac{1}{13} \int dz \int dz' \psi^2(z) \psi^2(z') * (13 + 13u - 14u^2 + 3u^3) e^{-u}, \quad (2.42)$$

where $u = q|\mathbf{z} - \mathbf{z}'|$.

The total acoustic phonon scattering rate can be written as:

$$\tau_{acp}^{-1}(E) = \tau_{DP}^{-1}(E) + \tau_{PE,l}^{-1}(E) + 2\tau_{PE,t}^{-1}(E), \quad (2.43)$$

where 2 means the two degenerate transverse acoustic phonon model.

2.4.3 Interface Roughness Scattering

The interface roughness scattering rate can be written as (Walukiewicz, 1992)

$$\tau_{IR}^{-1}(E) = \frac{m^* e^2 F_{eff} \Delta^2 \Lambda^2}{\hbar^3} \int_0^\pi S^2(q) (1 - \cos \theta) e^{-q^2 \Lambda^2 / 4} d\theta, \quad (2.44)$$

where $F_{eff} = (eN_s)/(2\epsilon_s\epsilon_0)$ is the effective field, N_s is the sheet carrier density (2DEG), ϵ_s is the static dielectric constants, Δ is the characteristic height of the roughness, Λ is the correlation length, $S(q)$ is the dielectric function, and $q = |\mathbf{k} - \mathbf{k}'|$ is the difference between two wave vector \mathbf{k} and \mathbf{k}' .

2.4.4 Electron–electron Coulomb Interactions

In addition to phonon and interface-related scattering mechanisms, electron–electron Coulomb interactions can also influence carrier transport, particularly in high-density two-

dimensional systems. These interactions give rise to scattering by collective charge oscillations, or interface plasmon modes, that can occur at boundaries between different dielectric materials. In MOS-like structures, electrons in the gate and channel can couple through long-range Coulomb forces, leading to significant momentum exchange even though individual electron–electron scattering events conserve momentum. This form of interaction has been shown to degrade mobility in ultra-thin oxide devices due to strong interlayer coupling. (Fischetti, 2001)

In this study, electron–electron Coulomb scattering is not included, for two primary reasons. First, the focus is limited to dominant phonon and interface-related mechanisms relevant to III-nitride heterostructures. Second, the doping concentration used in the GaN buffer layer ($N_d = 4 \times 10^{16} \text{ cm}^{-3}$) is not high enough for electron–electron interactions to significantly impact the overall scattering rate. Therefore, under the conditions modeled here, the influence of such Coulombic interactions is expected to be negligible.

2.4.5 Optical Phonon Scattering

For higher temperatures or in semiconductors with strong polar interactions, longitudinal optical (LO) phonon scattering becomes significant. The emission, absorption of LO phonon ($\hbar\omega_{LO}$) and the out-scattering rate can be written as (Bellotti et al., 2009; Yu and Brennan, 2001)

$$S_e(E) = \frac{e^2 m^* \omega_{LO}}{4\pi\epsilon_0 \hbar^2} \left[\frac{1}{\epsilon_\infty} - \frac{1}{\epsilon_s} \right] [N_q + 1 - f_0(E - \hbar\omega_{LO})] \sqrt{\frac{E - \hbar\omega_{LO}}{E}} \int_0^\pi \frac{H(q^-)}{q^-} \cos\theta d\theta \quad (2.45)$$

$$S_a(E) = \frac{e^2 m^* \omega_{LO}}{4\pi\epsilon_0 \hbar^2} \left[\frac{1}{\epsilon_\infty} - \frac{1}{\epsilon_s} \right] [N_q + f_0(E + \hbar\omega_{LO})] \sqrt{\frac{E + \hbar\omega_{LO}}{E}} \int_0^\pi \frac{H(q^+)}{q^+} \cos\theta d\theta \quad (2.46)$$

$$\begin{aligned}
S_o(E) = & \frac{e^2 m^* \omega_{LO}}{4\pi \epsilon_0 \hbar^2} \left[\frac{1}{\epsilon_\infty} - \frac{1}{\epsilon_s} \right] * \\
& \left\{ [N_q + 1 - f_0(E - \hbar \omega_{LO})] \int_0^\pi \frac{H(q^-)}{q^-} \cos \theta d\theta \right. \\
& \left. + [N_q + f_0(E + \hbar \omega_{LO})] \int_0^\pi \frac{H(q^+)}{q^+} \cos \theta d\theta \right\},
\end{aligned} \tag{2.47}$$

where ϵ_∞ and ϵ_s are the optical and static dielectric constants respectively, $N_q = 1/[\exp(\hbar \omega_{LO}/k_B T) - 1]$ is the optical phonon occupation number, $H(q^\pm)$ is the subband coupling coefficient defined in equation 2.35, and q^\pm ("±" means the absorption and emission of an optical phonon) is defined as

$$q^\pm = \frac{\sqrt{2m^*}}{\hbar} \sqrt{(2E(k) \pm \hbar \omega_{LO}) - 2\sqrt{E(k)[E(k) \pm \hbar \omega_{LO}]} \cos \theta} \tag{2.48}$$

The total optical phonon relaxation time can be written as,

$$\tau_{LO} = \frac{1}{S_o(E) - S_e(E) - S_a(E)} \tag{2.49}$$

2.4.6 Total scattering rate and Mobility

In realistic conditions, electrons in a 2DEG are scattered by both acoustic and optical phonons, as well as interface roughness. The overall scattering rate is obtained by summing the individual contributions,

$$\tau^{-1}(E) = \tau_{acp}^{-1}(E) + \tau_{LO}^{-1}(E) + \tau_{IR}^{-1}(E) \tag{2.50}$$

Within the relaxation time approximation, this total scattering rate can then be used to calculate the drift mobility (Yu and Brennan, 2001):

$$\mu = \frac{e}{m^*} \langle \tau(E) \rangle, \tag{2.51}$$

Parameter	Unit	Value
Mass density (ρ)	kg/m^3	6.1×10^3
Static Dielectric Constant (ϵ_s)	ϵ_0	10.4
Optical Dielectric Constant (ϵ_∞)	ϵ_0	5.35
Longitudinal Optical Phonon Energy ($\hbar\omega_{LO}$)	eV	0.095
Longitudinal Acoustic Phonon Velocity (v_l)	cm/s	6.6×10^5
Piezoelectric constant (h_{14})	V/cm	4.28×10^7
Longitudinal Elastic constant (c_l)	N/m^2	2.66×10^{11}
Transverse Elastic constant (c_t)	N/m^2	0.62×10^{11}

Table 2.2: Parameters used in the mobility calculation (Yu and Brennan, 2001; Hsu and Walukiewicz, 1997)

where $\langle \tau(E) \rangle$ indicates an average over the electron energy distribution, and it's defined as

$$\langle \tau^n \rangle = \frac{\int_0^\infty \tau^n E \frac{\partial f_0}{\partial E} dE}{\int_0^\infty E \frac{\partial f_0}{\partial E} dE} \quad (2.52)$$

Chapter 3

Results

3.1 Results of Self-Consistent Solver for the Heterostructure

The result of the conduction band profile for AlGa_N/Ga_N and ScAlN/GaN is shown in Figure 3.1 and 3.3, respectively. In Figures 3.1 and 3.3, the conduction band in Ga_N bends downward below the Fermi energy due to polarization-induced charges at the heterointerface, confining electrons in the quantum well and forming the two-dimensional electron gas (2DEG). As the temperature decreases, the electrons occupy lower energy states, causing the conduction band to bend more at lower temperatures. The lowest point of the conduction band is shown in Figures 3.2 and 3.4 for AlGa_N/Ga_N and ScAlN/GaN, respectively.

Detailed examination of the conduction band reveals the differences between the two heterostructure systems. At room temperature (300 K), the conduction band minimum in AlGa_N/Ga_N reaches approximately -0.82 eV below the Fermi level, while in ScAlN/GaN, it decreases significantly deeper to approximately -1.51 eV. This represents an strong quantum well depth, where the difference is caused by the significantly stronger polarization effects in the ScAlN/GaN system.

As listed in Table 2.1, the fundamental material parameters leading to these differences are the spontaneous polarization and piezoelectric constants. The spontaneous polarization in $Sc_{0.18}Al_{0.82}N$ ($1.238C/m^2$) exceeds that in $Al_{0.15}Ga_{0.85}N$ ($0.037C/m^2$). Even more, the piezoelectric constant e_{33} for $Sc_{0.18}Al_{0.82}N$ ($1.87 C/m^2$) is more than twice that of $Al_{0.15}Ga_{0.85}N$ ($0.84 C/m^2$). These enhanced polarization parameters generate stronger polarization-induced electric fields at the interface, leading to more band bending and

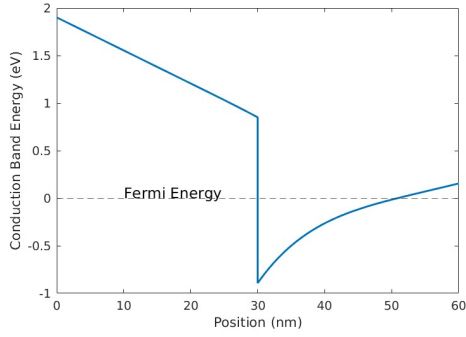


Figure 3.1: Conduction Band Energy of $Al_{0.15}Ga_{0.85}N/GaN$ at 300K

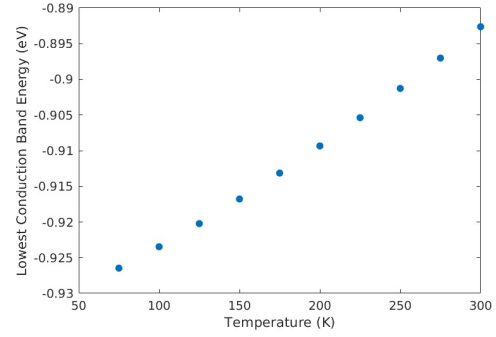


Figure 3.2: The Lowest Point of Conduction Band in $Al_{0.15}Ga_{0.85}N/GaN$

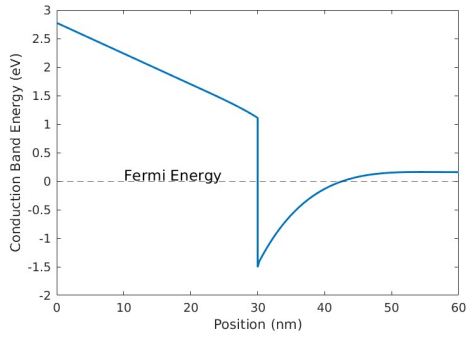


Figure 3.3: Conduction Band Energy of $Sc_{0.18}Al_{0.82}N/GaN$ at 300K

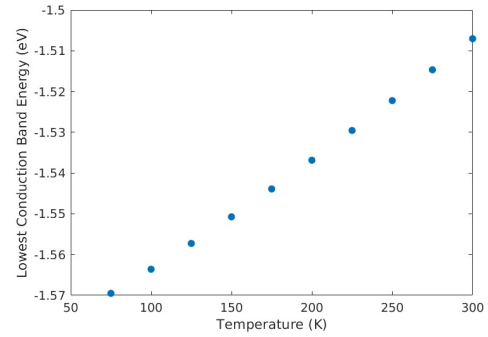


Figure 3.4: The Lowest Point of Conduction Band in $Sc_{0.18}Al_{0.82}N/GaN$

deeper quantum wells.

The temperature dependence of the conduction band minimum, illustrated in Figures 3.2 and 3.4, shows important physics in these heterostructures. Our self-consistent calculations show that as temperature decreases from 300 K to 75 K, the conduction band minimum in AlGa_{0.85}N/GaN decreases by approximately 36.53 meV, while in ScAlN/GaN, it decreases by approximately 62.47 meV. This temperature-dependent enhancement of band bending arises from the reason that as temperature decreases, the Fermi-Dirac distribution narrows, causing electrons to occupy lower energy states with higher probability.

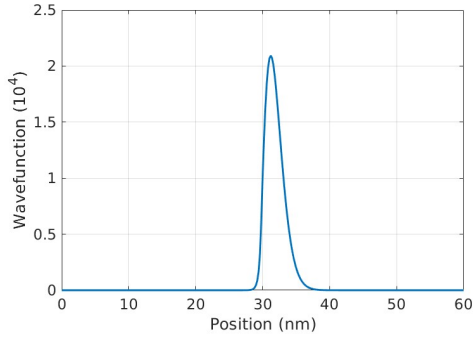


Figure 3-5: Ground State Wave Function of AlGaN/GaN at 300K

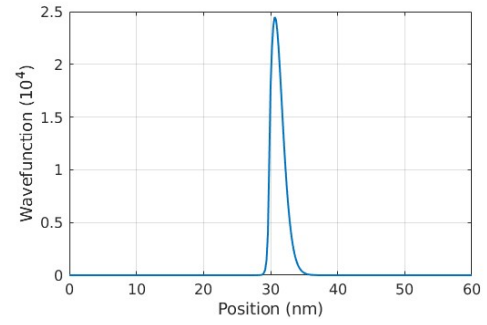


Figure 3-6: Ground State Wave Function of ScAlN/GaN at 300K

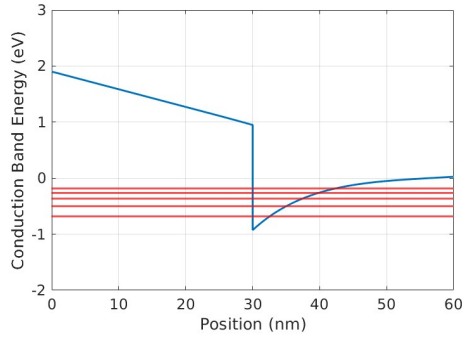


Figure 3-7: Conduction Band Energy with First Five Subband Energy of AlGaN/GaN at 50K

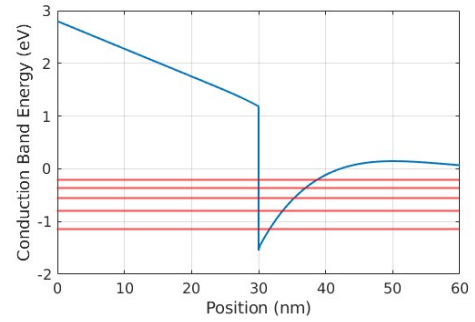


Figure 3-8: Conduction Band Energy with First Five Subband Energy of ScAlN/GaN at 150K

The deeper conduction band well in ScAlN/GaN directly impacts the 2DEG characteristics. Based on our calculations, the sheet carrier concentration in ScAlN/GaN reaches $n_s \approx 5.3 \times 10^{13} \text{ cm}^{-2}$, significantly exceeding the typical values of $n_s \approx 1.1 \times 10^{13} \text{ cm}^{-2}$ observed in AlGaN/GaN. This enhancement arose from higher polarization-induced sheet charge density. The substantially deeper conduction band minimum in ScAlN/GaN, resulting from enhanced spontaneous and piezoelectric polarization, creates stronger electron confinement and higher sheet carrier densities. This can be observed from the magnitude of wavefunction of Ground State, which is shown in Figure 3-5 and 3-6. The ground state wavefunction amplitude in the ScAlN/GaN heterostructure exhibits a significantly

higher peak value of approximately 2.5×10^4 compared to only around 2.0×10^4 in AlGa_N/Ga_N structures. This enhanced wavefunction amplitude correlates directly with the greater carrier concentration induced by the stronger spontaneous and piezoelectric polarization fields of ScAlN. The increased electron density at the interface leads to more pronounced electron-electron interactions and enhanced scattering events. Consequently, we can predict lower electron mobility in ScAlN/GaN heterostructures compared to their AlGa_N/Ga_N counterparts, as the higher carrier density inherently results in more frequent scattering processes. The first five subbands' energy of AlGa_N/Ga_N and ScAlN/GaN is shown in Figure 3.7 and 3.8 respectively, for two certain temperature for example, which we will use to calculate the scattering rate of inter- and intra- subband absorption and emission for each scattering mechanism.

3.2 Results of Mobility

The result of mobility in $Al_xGa_{1-x}N/GaN$ and $Sc_xAl_{1-x}N/GaN$ are shown in Figure 3.9 and 3.11 respectively.

3.2.1 AlGa_N/Ga_N Result

Electron mobility in AlGa_N/Ga_N heterostructures exhibits distinct temperature-dependent behavior across different scattering mechanisms, which is shown in Figure 3.9, and for each scattering rate, the result is shown in Figure 3.10.

The deformation potential (DP) mechanism illustrates the highest mobility values throughout the temperature range, starting at $2.935 \times 10^5 \text{ cm}^2/Vs$ at 300K and increasing to $2.677 \times 10^7 \text{ cm}^2/Vs$ at 50K. These elevated values indicate that DP scattering has minimal impact on limiting electron transport in these structures, as higher mobility values correspond to less restrictive scattering. As shown in Figure 3.10(a), the DP scattering rate exhibits a characteristic energy dependence at low energies, reaching approximately

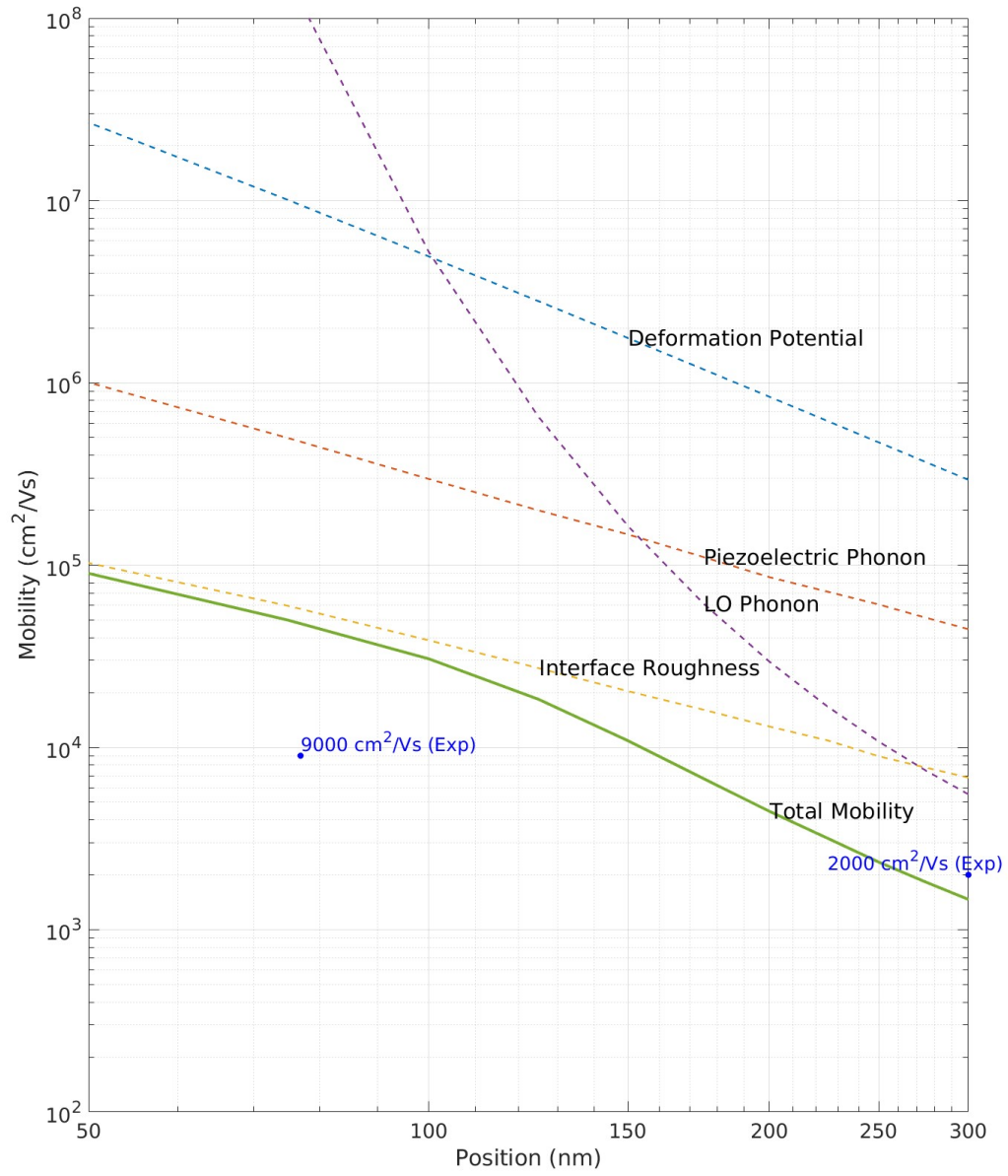


Figure 3.9: Mobility of *AlGaIn/GaN* under different temperature, where "." is the experimental data.

$3.0 \times 10^{10} \text{ s}^{-1}$ at 0.05 eV, which explains its reduced impact on overall transport. This behavior arises from the \sqrt{E} dependence in the density of states coupled with the linear energy dependence in the scattering probability, leading to the parabolic profile visible in the figure. Piezoelectric (PZ) scattering demonstrates mobility values of $4.453 \times 10^4 \text{ cm}^2/\text{Vs}$ at room temperature, rising to $1.005 \times 10^6 \text{ cm}^2/\text{Vs}$ at 50K. The difference between DP and PZ mobility narrows significantly at higher temperatures, suggesting that piezoelectric effects become proportionally more important near room temperature. Figure 3.10(b) reveals that the piezoelectric scattering rate exhibits a strong energy dependence. This enhanced scattering strength at low energies is a direct consequence of the fundamental $1/q$ dependence of the piezoelectric interaction, where q is the phonon wavevector. However, despite this characteristic $1/q$ dependence, our calculations show that piezoelectric scattering remains relatively weak compared to LO-phonon scattering and interface roughness scattering, contributing minimally to the overall mobility limitation across the temperature range.

Interface roughness (IR) scattering presents substantially lower mobility values of $6824 \text{ cm}^2/\text{Vs}$ at 300K, increasing to $1.027 \times 10^5 \text{ cm}^2/\text{Vs}$ at 50K, with a characteristic height of the roughness $(\Delta) = 0.6 \text{ nm}$ and correlation length $(\Lambda) = 1.5 \text{ nm}$. These comparatively low numbers indicate that interface roughness significantly limits overall carrier transport, especially at lower temperature. The relatively slow increase in IR mobility at lower temperatures reveals its strong influence across all temperature regimes. The interface roughness scattering rate shown in Figure 3.10(e) displays a steep energy dependence, increasing rapidly until approximately 0.05 eV before exhibiting a saturation behavior at higher energies. This saturation occurs because higher-energy electrons, while having greater scattering probability, spend proportionally less time near the interface due to their increased velocity. The maximum value at approximately $2.8 \times 10^{13} \text{ s}^{-1}$ demonstrates why IR scattering becomes the dominant limitation at low temperatures where carriers occupy lower

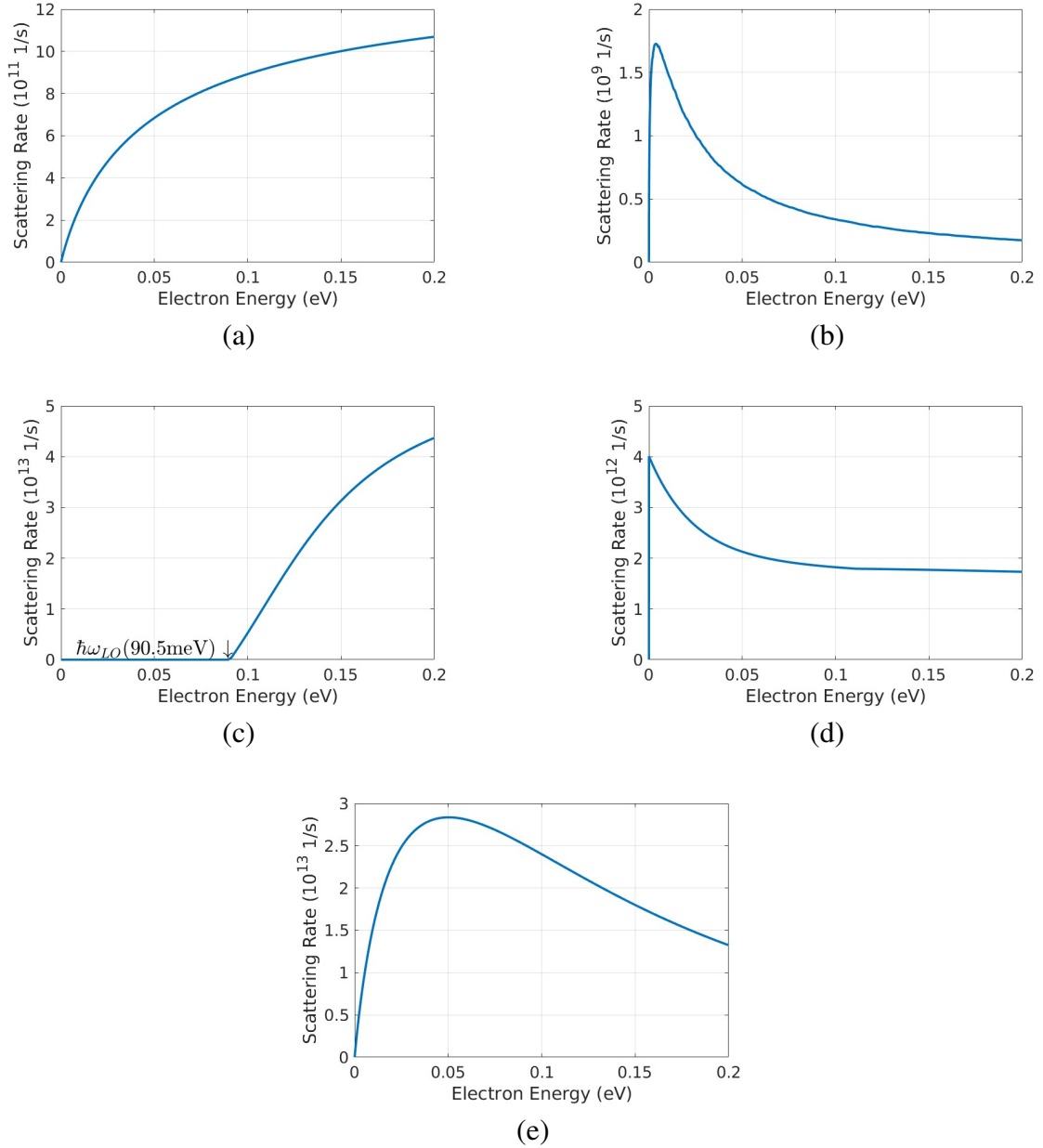


Figure 3-10: Scattering Rate of AlGaIn/GaN at 300K: (a)Deformation Potential (b)Piezoelectric Phonon (c)Emission of LO phonon (d)Absorption of LO phonon (e)Interface Roughness, the Electron Energy is measured from the bottom of the first subband to second subband

energy states.

Longitudinal optical (LO) phonon scattering shows mobility values of approximately $5530 \text{ cm}^2/\text{Vs}$ at 300K, rising dramatically to $1.8 \times 10^{11} \text{ cm}^2/\text{Vs}$ at 50K. At room temperature, this mechanism imposes the most severe limitation on electron transport, with mobility values lower than interface roughness. However, LO scattering becomes nearly insignificant at lower temperatures, where its mobility exceeds that of IR scattering. Figures 3-10(c) and 3-10(d) illustrate the emission and absorption components of LO phonon scattering, respectively. The emission process (c) exhibits a characteristic threshold behavior, becoming significant only when electrons possess sufficient energy ($\sim 90.5 \text{ meV}$) to emit an LO phonon, explaining the sharp increase in scattering rate at this energy. In contrast, the absorption process (d) shows non-zero values even at low energies but with reduced magnitude at 300K, reflecting the phonon occupation number proportional to the Bose-Einstein distribution. The combined effect produces scattering rates exceeding 10^{13} s^{-1} at higher energies, which explains why LO phonon scattering dominates at room temperature.

The calculated total mobility reaches $1466 \text{ cm}^2/\text{Vs}$ at 300K, showing reasonable agreement with experimental measurements of approximately $2000 \text{ cm}^2/\text{Vs}$. (Gaska et al., 1999) As temperature decreases, the total mobility curve gradually approaches the interface roughness mobility curve, becoming nearly identical at temperatures below 75K where both reach approximately $9.006 \times 10^4 \text{ cm}^2/\text{Vs}$ at 50K. This behavior clearly shows how the dominant scattering mechanism shifts from a combination of LO phonon and interface roughness scattering at room temperature to predominantly interface roughness scattering at low temperatures. This transition occurs because phonon scattering weakens considerably as temperature drops, while interface roughness effects remain relatively constant across the temperature range.

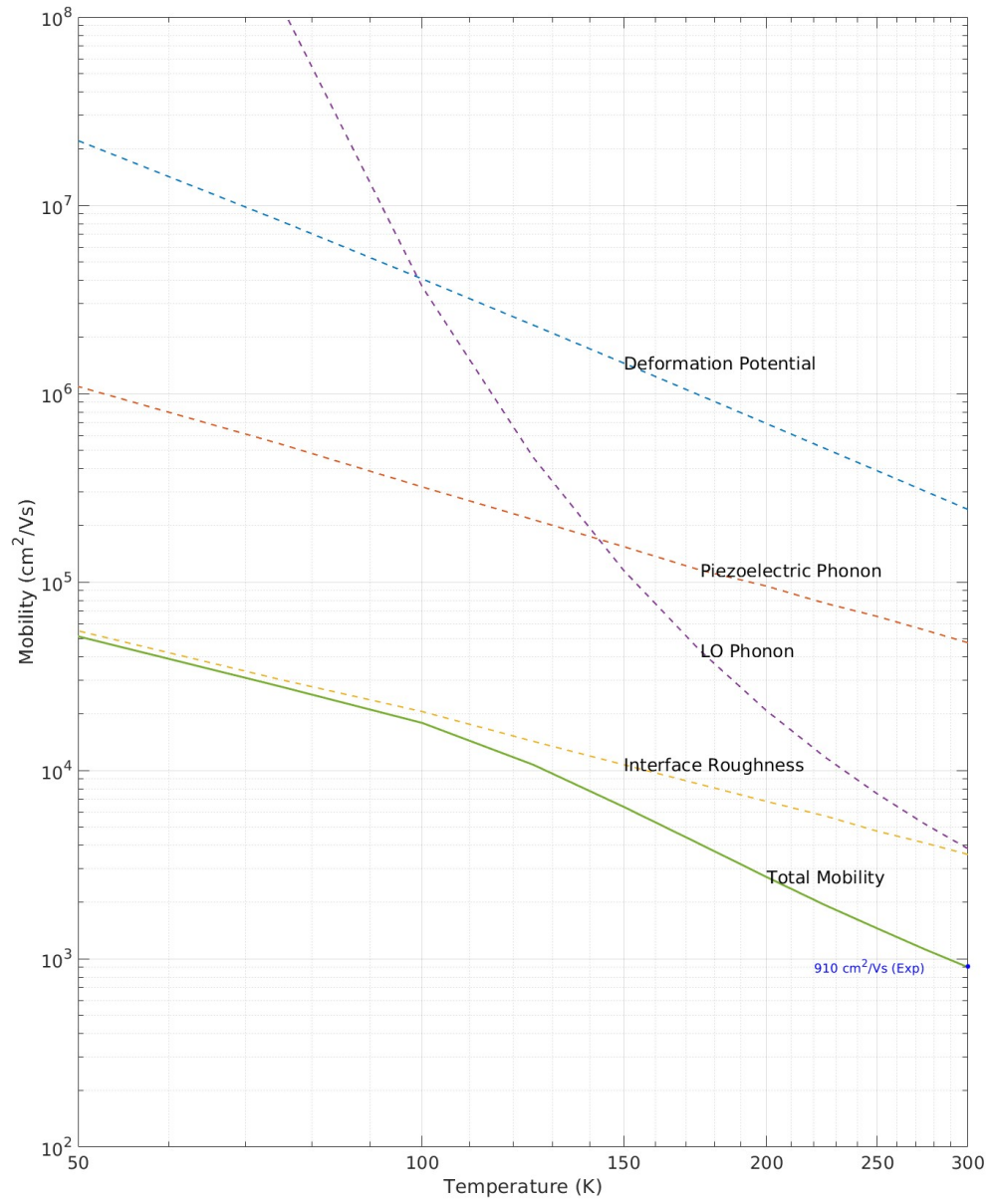


Figure 3-11: Mobility of $ScAlN/GaN$ under different temperature, where "." is the experimental data

3.2.2 ScAlN/GaN Result

Figure 3.11 presents the calculated temperature dependence of electron mobility in ScAlN/GaN heterostructures from 50 K to 300 K. The data reveals a clear trend of decreasing mobility with increasing temperature, which is characteristic of doped semiconductors. For each scattering mechanism, the corresponding energy-dependent scattering rates are illustrated in Figure 3.12.

At room temperature (300 K), the total electron mobility in our ScAlN/GaN structure is $901.1 \text{ cm}^2/\text{Vs}$, showing values with experimental measurements of approximately $910 \text{ cm}^2/\text{Vs}$ (Hardy et al., 2017), which progressively increases as temperature decreases, reaching $5.14 \times 10^4 \text{ cm}^2/\text{Vs}$ at 50 K. This strong temperature dependence reflects the changing dominance of different scattering mechanisms across the temperature range. Longitudinal optical (LO) phonon scattering dominates at high temperatures, as evidenced by the rapid increase in total mobility as temperature decreases. From our simulations, LO-phonon-limited mobility increases from $3836 \text{ cm}^2/\text{Vs}$ at 300 K to $3.87 \times 10^{10} \text{ cm}^2/\text{Vs}$ at 50 K. This dramatic enhancement reflects the rapid decrease in phonon occupation number as temperature drops, resulting in significantly reduced electron-phonon scattering events. Figures 3.12(c) and 3.12(d) illustrate the emission and absorption components of LO phonon scattering, respectively. The emission process demonstrates a distinct threshold behavior at the LO phonon energy (90.5 meV), with scattering rates rapidly increasing to approximately $1.0 \times 10^{14} \text{ s}^{-1}$ beyond this energy. The absorption process, while active across all energies, shows stronger magnitude at higher energies. When emission and absorption processes are combined, the total LO-phonon scattering rate reaches values exceeding 10^{14} s^{-1} at room temperature, approximately two orders of magnitude higher than acoustic phonon mechanisms. This dominant scattering rate explains why LO-phonon-limited mobility becomes the primary transport limitation as temperature increases.

Interface roughness scattering, with $\Delta = 0.9 \text{ nm}$ and $\Lambda = 1.5 \text{ nm}$ in our model, shows a

weaker temperature dependence. The interface-roughness-limited mobility increases from $3576 \text{ cm}^2/\text{Vs}$ at 300 K to $5.5 \times 10^4 \text{ cm}^2/\text{Vs}$ at 50 K. At low temperatures ($\leq 75 \text{ K}$), we observe that the total mobility ($2.7 \times 10^4 \text{ cm}^2/\text{Vs}$ at 75 K) approaches the interface roughness-limited mobility ($3.0 \times 10^4 \text{ cm}^2/\text{Vs}$ at 75 K), indicating that interface roughness becomes the dominant limiting mechanism at these temperatures.

At room temperature, the total mobility ($901 \text{ cm}^2/\text{Vs}$) is closer to interface-roughness-scattering-limited mobility ($3576 \text{ cm}^2/\text{Vs}$) and LO-phonon-limited mobility ($3836 \text{ cm}^2/\text{Vs}$), indicating that both interface roughness scattering and LO-phonon scattering are the main factors in contributing to total mobility. Figure 3.12(e) reveals that the interface roughness scattering rate increases sharply at low energies, reaching approximately $5.5 \times 10^{13} \text{ s}^{-1}$ at 0.05 eV before exhibiting a more gradual increase at higher energies. This energy profile explains why interface roughness dominates at low temperatures where the thermal distribution keeps carriers near the subband minimum.

Piezoelectric scattering shows an increase from approximately $4.76 \times 10^4 \text{ cm}^2/\text{Vs}$ at 300 K to $1.09 \times 10^6 \text{ cm}^2/\text{Vs}$ at 50 K. The large piezoelectric constants in ScAlN ($e_{33} = 1.91 \text{ C/m}^2$) generate significant strain-related scattering, though its impact is less notable than interface roughness at most temperatures. The piezoelectric scattering rate in Figure 3.12(b) demonstrates a distinctive energy dependence, with the stronger activity at lower energies reflecting the $1/q$ dependence, where q is the phonon wave vector.

Deformation potential scattering demonstrates the weakest temperature dependence among the major scattering mechanisms. Our data indicates deformation-potential-limited mobility increases from approximately $2.4 \times 10^5 \text{ cm}^2/\text{Vs}$ at 300 K to $2.2 \times 10^7 \text{ cm}^2/\text{Vs}$ at 50 K. This extraordinarily high mobility at low temperatures means that deformation potential scattering becomes negligible compared to other mechanisms as temperature decreases. This is expected as deformation potential scattering is directly related to thermal lattice vibrations.

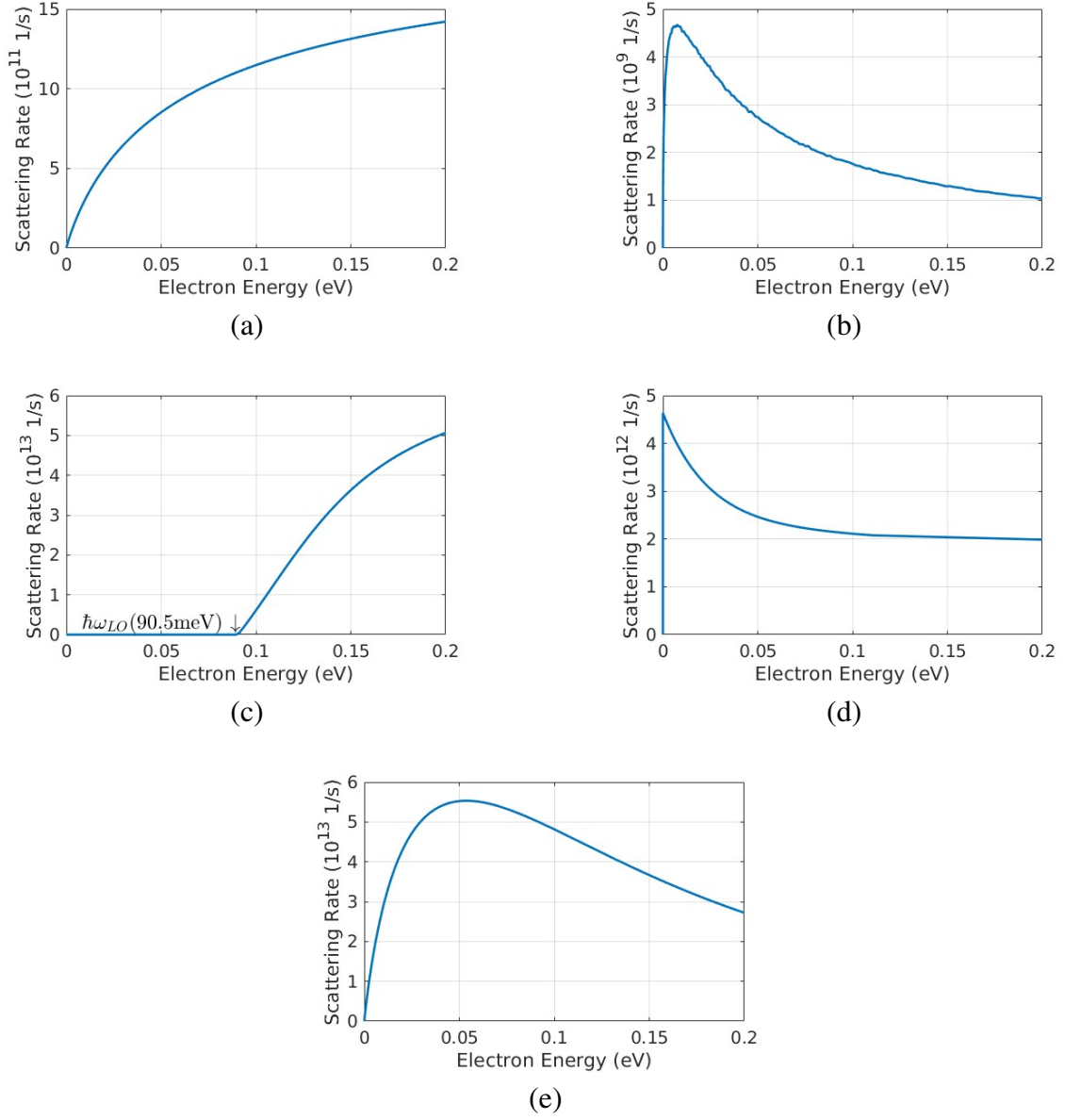


Figure 3-12: Scattering Rate of ScAlN/GaN at 300K: (a) Deformation Potential (b) Piezoelectric Phonon (c) Emission of LO phonon (d) Absorption of LO phonon (e) Interface Roughness, the Electron Energy is measured from the bottom of the first subband to second subband

A crucial crossover in dominant scattering mechanisms occurs around 150-175 K, where the mobility increases from $4051 \text{ cm}^2/\text{Vs}$ at 175 K to $6401 \text{ cm}^2/\text{Vs}$ at 150 K. This temperature range marks the transition from phonon-dominated scattering at higher temperatures to interface-roughness-dominated scattering at lower temperatures. This crossover is clearly visible in the figure 3.11, where the mobility values at low temperatures nearly converge with the interface roughness-limited mobility. The energy-dependent scattering rates in Figure 3.12 provide the physical basis for this crossover: as temperature decreases, the average electron energy decreases, shifting the electron distribution toward the subband minimum where interface roughness scattering is more effective (as shown by the steep initial slope in Figure 3.12(e)). Simultaneously, the LO phonon absorption rate drops dramatically due to reduced phonon occupation numbers, while emission processes become increasingly restricted to the shrinking fraction of electrons with energies exceeding the LO phonon energy threshold. This energy-dependent interplay, coupled with the different temperature scaling of each mechanism, produces the characteristic crossover behavior that defines the optimal temperature range for device operation.

3.2.3 Comparison between AlGaIn/GaN and ScAlIn/GaN

At room temperature (300 K), the total electron mobility in ScAlIn/GaN reaches $901.1 \text{ cm}^2/\text{Vs}$, which is notably lower than that observed in AlGaIn/GaN structures ($1466 \text{ cm}^2/\text{Vs}$ using the high-temperature approximation). This difference suggests that despite the enhanced polarization characteristics of ScAlIn, the AlGaIn/GaN system demonstrates superior room temperature carrier transport. At lower temperatures (50 K), AlGaIn/GaN maintains its advantage with a low-temperature mobility of approximately $9.0 \times 10^4 \text{ cm}^2/\text{Vs}$ compared to $5.14 \times 10^4 \text{ cm}^2/\text{Vs}$ for ScAlIn/GaN.

The scattering mechanism shows similar characteristic in these materials. In AlGaIn/GaN, polar optical phonon scattering imposes a major limitation at room temperature, with the mobility of approximately $5530 \text{ cm}^2/\text{Vs}$, whereas interface roughness con-

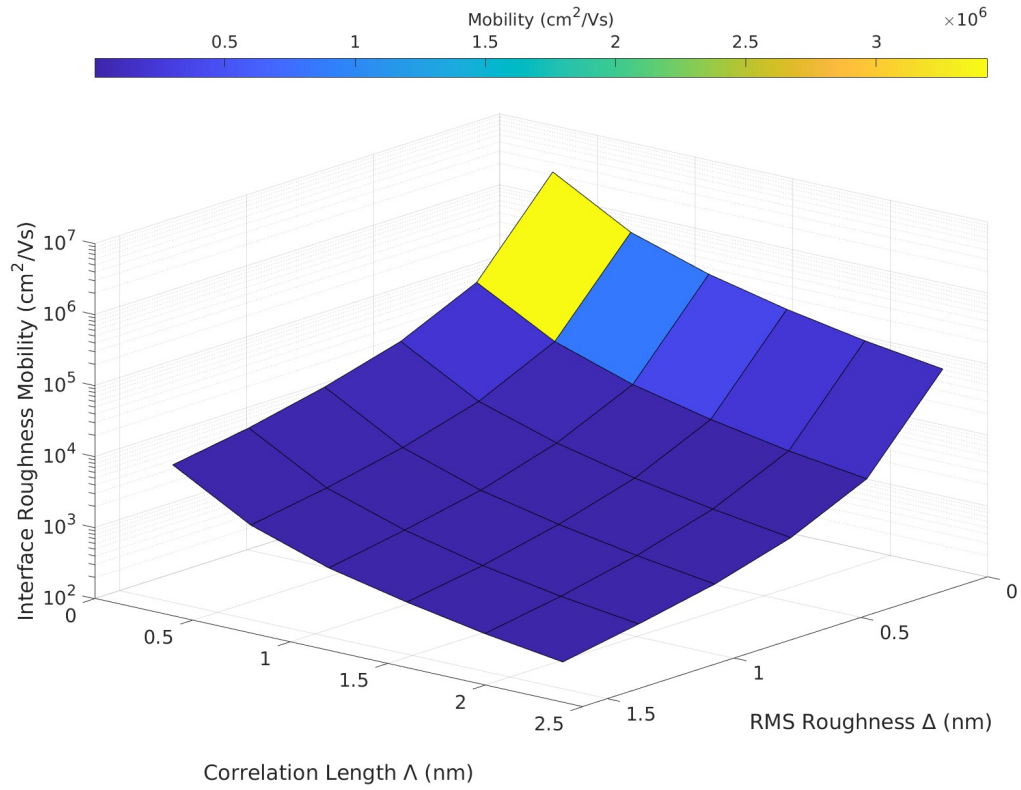


Figure 3-13: Interface Roughness mobility with different parameter Δ and Λ in AlGaIn/GaN

tributes a similar but higher mobility limit of $6824 \text{ cm}^2/\text{Vs}$. This showed similar characteristic with ScAlN/GaN, while interface roughness emerges as more restrictive at room temperature ($3576 \text{ cm}^2/\text{Vs}$) than polar optical phonon scattering ($3836 \text{ cm}^2/\text{Vs}$). This suggests that both optical-phonon-scattering and interface-roughness-scattering in AlGaIn/GaN and ScAlN/GaN play critical roles in these devices at room temperature.

3.2.4 Interface Roughness Effects on 2DEG Transport

Interface roughness scattering plays a fundamental role in limiting carrier transport in AlGaIn/GaN and ScAlN/GaN heterostructures, with mobility values exhibiting extraordinary sensitivity to nanoscale interfacial quality parameters. Our parametric analysis (Figure 3-13) reveals that AlGaIn/GaN systems demonstrate interface roughness-limited mobility

ranging from 3.43×10^6 to $372 \text{ cm}^2/\text{Vs}$ at 300K across the parameter space ($\Delta = 0.1\text{-}1.6 \text{ nm}$, $\Lambda = 0.4\text{-}2.4 \text{ nm}$), while ScAlN/GaN exhibits a similar but slightly enhanced range from 4.02×10^6 to $449 \text{ cm}^2/\text{Vs}$ under identical conditions. This suggests marginally better interface quality potential in ScAlN structures despite their generally higher carrier densities.

The mobility's extraordinary sensitivity to interface parameters is evident in both material systems—when roughness height (Δ) increases from 0.1 to 1.6 nm at fixed correlation length ($\Lambda = 0.4 \text{ nm}$), mobility decreases from 3.43×10^6 to $1.34 \times 10^4 \text{ cm}^2/\text{Vs}$ in AlGaIn/GaN and from 2.28×10^7 to $8.78 \times 10^4 \text{ cm}^2/\text{Vs}$ ScAlN/GaN. The mobility exhibits strong scaling relationships with both parameters, decreasing approximately proportional to Δ^{-2} for fixed correlation lengths, as evidenced by the systematic decrease from 3.82×10^5 to $1460 \text{ cm}^2/\text{Vs}$ when Δ increases from 0.1 to 1.6 nm while maintaining $\Lambda = 1.2 \text{ nm}$ in AlGaIn/GaN, and from 4.51×10^5 to $1742.21 \text{ cm}^2/\text{Vs}$ in ScAlN/GaN. Similarly, the correlation length dependence is evident in the drop from 6.87×10^4 to $1952 \text{ cm}^2/\text{Vs}$ when Λ increases from 0.4 to 2.4 nm with fixed $\Delta = 0.7 \text{ nm}$ in AlGaIn/GaN, and from 8.16×10^4 to $2383.9 \text{ cm}^2/\text{Vs}$ in ScAlN/GaN. The details of the parameter dependence is shown in Figure 3.14 ~ 3.17. The product term $\Delta^2\Lambda^2$ in the scattering rate formula explains this compound effect, where both parameters impact carrier mobility.

The temperature dependence of interface roughness scattering reveals additional insights. At 100 K, the same parameter range ($\Delta : 0.1\text{--}1.6 \text{ nm}$, $\Lambda : 0.4\text{--}2.4 \text{ nm}$) produces mobility values spanning from 2.01×10^7 to $2153 \text{ cm}^2/\text{Vs}$, while at 50 K, this range narrows to 5.35×10^7 to $5856 \text{ cm}^2/\text{Vs}$. This convergence at lower temperatures occurs because other scattering mechanisms diminish more rapidly than interface roughness scattering, making the latter increasingly dominant while its own temperature sensitivity decreases.

These quantitative findings demonstrate the critical importance of nanometer-scale interface quality control in III-nitride heterostructures, particularly for applications operating

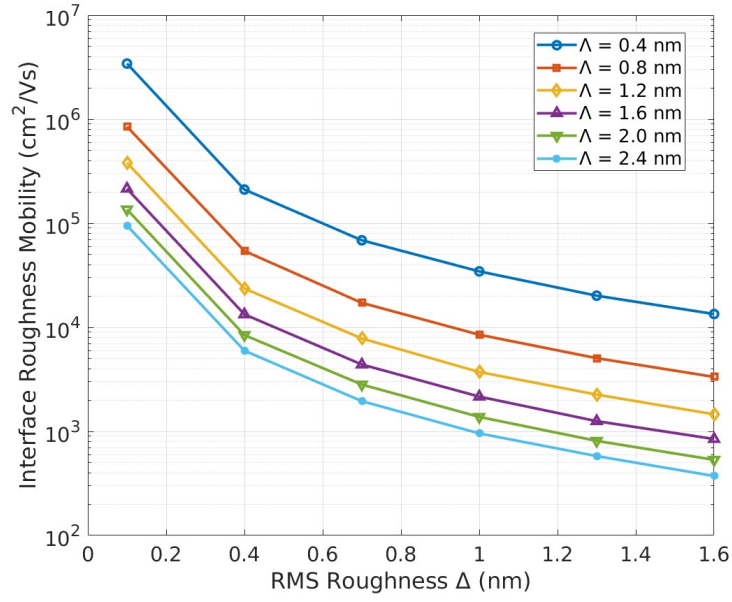


Figure 3-14: Effect of Roughness Height on Mobility (300K) of Al-GaN/GaN Interface

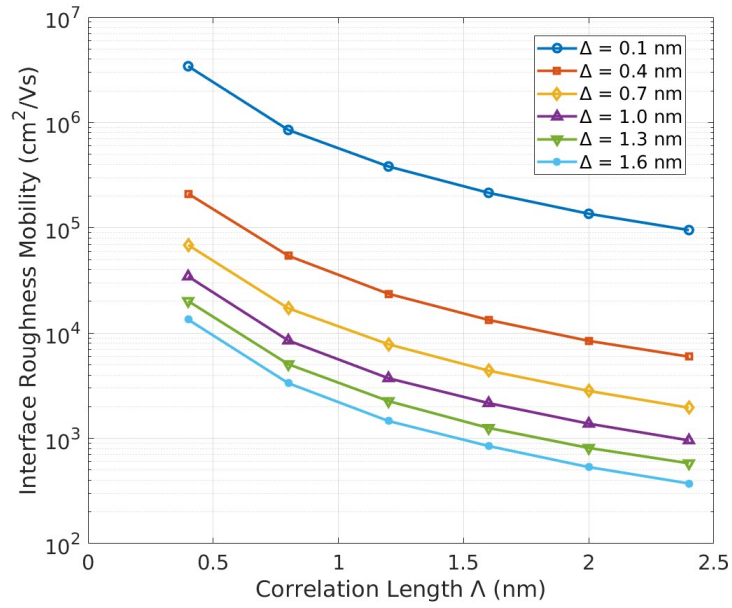


Figure 3-15: Effect of Correlation Length on Mobility (300K) of Al-GaN/GaN Interface

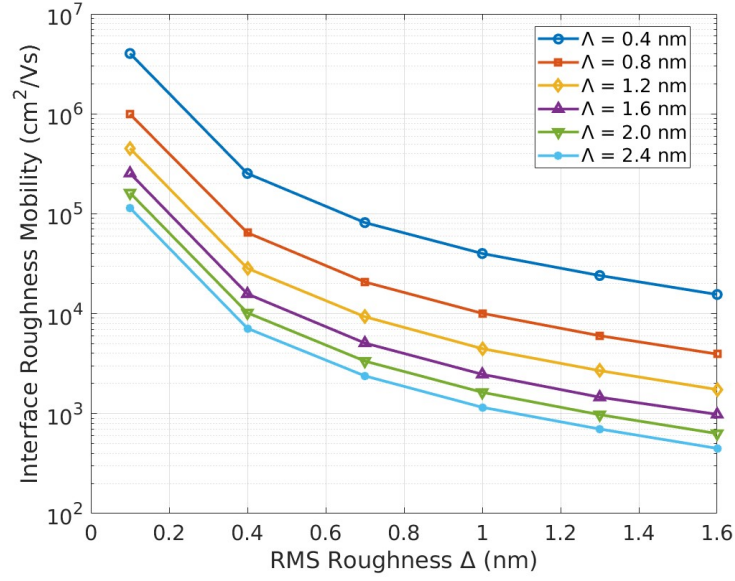


Figure 3-16: Effect of Roughness Height on Mobility (300K) of ScAlN/GaN Interface

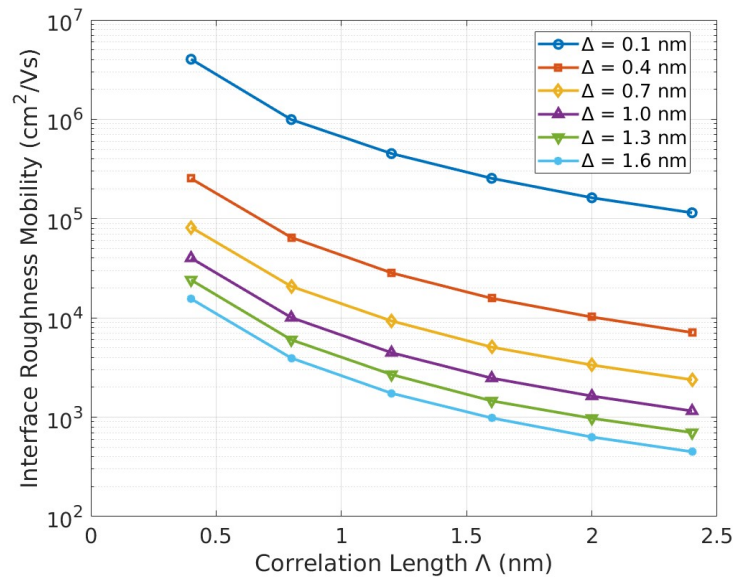


Figure 3-17: Effect of Correlation Length on Mobility (300K) of ScAlN/GaN Interface

at or near room temperature where the effect of interface roughness on overall device performance becomes increasingly significant relative to other scattering mechanisms.

Chapter 4

Conclusions

In this thesis, We have conducted a detailed quantum-mechanical study on the electron transport properties in AlGa_N/Ga_N and ScAlN/GaN heterostructures, showing differences in their electronic features and transport processes. Solving self-consistently the coupled Poisson-Schrödinger equations and through elaborate modeling of several scattering mechanisms, we have shown how the enhanced polarization effects in ScAlN/GaN systems impact quantum confinement, carrier distribution, and therefore electron mobility.

Our result suggests the ScAlN/GaN heterostructure has approximately 62% greater spontaneous polarization and more than double the piezoelectric constant compared to AlGa_N/Ga_N. These stronger polarization effects, combined with the corresponding enhanced anisotropic deformation potentials, lead to much deeper quantum wells: in ScAlN/GaN, the conduction band minimum dips approximately 1.51 eV below the Fermi level, while in AlGa_N/Ga_N it only reaches 0.82 eV at room temperature. This deeper confinement directly leads to higher sheet carrier densities in ScAlN/GaN ($\sim 5.3 \times 10^{13} \text{ cm}^{-2}$) versus AlGa_N/Ga_N ($\sim 1.1 \times 10^{13} \text{ cm}^{-2}$). Despite these stronger polarization effects and higher carrier densities, our calculations showed that ScAlN/GaN exhibits lower electron mobility than AlGa_N/Ga_N under all temperature regime. At 300K, the mobility of ScAlN/GaN is $901.1 \text{ cm}^2/\text{Vs}$ compared to $1466 \text{ cm}^2/\text{Vs}$ of AlGa_N/Ga_N, while at 50K, ScAlN/GaN still showed a lower mobility of $5.14 \times 10^4 \text{ cm}^2/\text{Vs}$ while AlGa_N/Ga_N reaches $9.0 \times 10^4 \text{ cm}^2/\text{Vs}$.

Our detailed analysis of scattering mechanisms reveals that longitudinal optical (LO)

phonon scattering dominates at higher temperatures in both heterostructures, with scattering rates reaching $10^{13} \sim 10^{14} \text{ s}^{-1}$ near room temperature. As temperature decreases, a transition occurs around 150-175K where interface roughness scattering becomes the dominant mobility-limiting mechanism.

Particularly, we found that interface roughness plays a critical role in determining electron mobility in both heterostructure systems, showing extraordinary sensitivity to nanoscale interface parameters. Our parametric analysis demonstrates that mobility scales approximately as $\Delta^{-2}\Lambda^{-2}$ (where Δ is roughness height and Λ is the correlation length). At room temperature, interface roughness-limited mobility can vary from $10^6 \text{ cm}^2/Vs$ to less than $10^3 \text{ cm}^2/Vs$ across the parameter space. This extreme sensitivity shows the critical importance of interface quality control for optimizing device performance. The temperature dependence analysis reveals that while individual scattering mechanisms scale differently with temperature, both heterostructures show a convergence toward interface roughness-limited mobility at low temperatures, regardless of interface parameters. This convergence indicates that efforts to improve low-temperature device performance should focus primarily on optimizing interface quality rather than other material parameters.

The findings impact the design and use of devices utilizing III-nitrides in significant ways. ScAlN/GaN exhibits much higher sheet carrier densities due to enhanced polarization effects, yet the reduction in mobility presents a design trade-off. For some systems where the current density and the power handling are major figures of merit, ScAlN/GaN may have some benefits despite having low mobility. On the other hand, for some systems where high frequency operation is moderately essential, AlGaN/GaN with its higher mobility can be more appropriate.

In conclusion, this comprehensive investigation of electron transport in AlGaN/GaN and ScAlN/GaN heterostructures provides fundamental insights into the polarization-enhanced quantum confinement and scattering-limited mobility in these promising material

systems. The quantitative understanding of scattering mechanisms and their temperature dependence established in this work provides valuable guidance for optimizing the design and fabrication of next-generation III-nitride electronic devices for high-power, high-frequency, and high-temperature applications.

References

- Ambacher, O., Foutz, B., Smart, J., Shealy, J. R., Weimann, N. G., Chu, K., Murphy, M., Sierakowski, A. J., Schaff, W. J., Eastman, L. F., Dimitrov, R., Mitchell, A., and Stutzmann, M. (2000). Two dimensional electron gases induced by spontaneous and piezoelectric polarization in undoped and doped algan/gan heterostructures. *Journal of Applied Physics*, 87(1):334–344.
- Ambacher, O., Smart, J., Shealy, J. R., Weimann, N. G., Chu, K., Murphy, M., Schaff, W. J., Eastman, L. F., Dimitrov, R., Wittmer, L., Stutzmann, M., Rieger, W., and Hilsenbeck, J. (1999). Two-dimensional electron gases induced by spontaneous and piezoelectric polarization charges in n- and ga-face algan/gan heterostructures. *Journal of Applied Physics*, 85(6):3222–3233.
- Bellotti, E., Driscoll, K., Moustakas, T. D., and Paiella, R. (2009). Monte carlo simulation of terahertz quantum cascade laser structures based on wide-bandgap semiconductors. *Journal of Applied Physics*, 105(11):113103.
- Bransden, B. H., Joachain, C. J. C. J., and Bransden, B. H. (2000). *Quantum mechanics*. Prentice Hall, Harlow, England ;, 2nd ed. edition.
- Chuang, S. L. (2009). *Physics of Photonic Devices*. Wiley Publishing, 2 edition.
- Fischetti, M. V. (2001). Long-range coulomb interactions in small si devices. part ii. effective electron mobility in thin-oxide structures. *Journal of Applied Physics*, 89(2):1232–1250.
- Gaska, R., Shur, M. S., Bykhovski, A. D., Orlov, A. O., and Snider, G. L. (1999). Electron mobility in modulation-doped algan–gan heterostructures. *Applied Physics Letters*, 74(2):287–289.
- Gunna, S., Bertazzi, F., Paiella, R., and Bellotti, E. (2007). *Nitride Semiconductor Devices*, chapter 06. WILEY-VCH Verlag GmbH Co. KGaA.
- Halpern, A. M., Ge, Y., and Glendening, E. D. (2022). Visualizing solutions of the one-dimensional schrödinger equation using a finite difference method. *Journal of Chemical Education*, 99(8):3053–3060.
- Hardy, M. T., Downey, B. P., Nepal, N., Storm, D. F., Katzer, D. S., and Meyer, D. J. (2017). Epitaxial scaln grown by molecular beam epitaxy on gan and sic substrates. *Applied Physics Letters*, 110(16):162104.

- Hsu, L. and Walukiewicz, W. (1997). Electron mobility in $\text{Al}_x\text{Ga}_{1-x}\text{N}/\text{GaN}$ heterostructures. *Physical Review. B*, 56:1520–1528.
- Kawamura, T. and Das Sarma, S. (1992). Phonon-scattering-limited electron mobilities in $\text{Al}_x\text{Ga}_{1-x}\text{As}/\text{GaAs}$ heterojunctions. *Physical Review. B*, 45:3612–3627.
- Walukiewicz, W. (1992). *Carrier Transport in Artificially Structured Two-Dimensional Semiconductor*. World Scientific Publishing Co. PTE Ltd.
- Yassine, M., Yassine, A., Nair, A., Sundarapandian, B., Afshar, N., Kirste, L., Fichtner, S., and Ambacher, O. (2024). Modeling of polarization reversal-induced interface sheet charge in wurtzite-type AlScN/GaN heterostructures. *Journal of Applied Physics*, 135(15):155702.
- Yoon, K. S., Stringfellow, G. B., and Huber, R. J. (1987). Monte carlo calculation of velocity-field characteristics in GaInAs/InP and $\text{GaInAs}/\text{AlInAs}$ single-well heterostructures. *Journal of Applied Physics*, 62(5):1931–1936.
- Yu, T.-H. and Brennan, K. F. (2001). Theoretical study of the two-dimensional electron mobility in strained InGaN -nitride heterostructures. *Journal of Applied Physics*, 89(7):3827–3834.
- Zaman, M. A. (2022). Numerical solution of the poisson equation using finite difference matrix operators. *Electronics*, 11(15):2365.

CURRICULUM VITAE

Contact Information

- **Name:** Bo-Shiang Yang
- **Email:** yboshian@bu.edu

Education

Boston University

Degree: MS in Electrical and Computer Engineering

Location: Boston, MA

Duration: Fall 2023 – May 2025

National Yang Ming Chiao Tung University

Degree: Bachelor in System Engineering, Division of Electrical and Electronic Engineering

Location: Taiwan

Duration: Fall 2019 – May 2023